Cell Systems

Diploid hepatocytes drive physiological liver renewal in adult humans

Graphical abstract

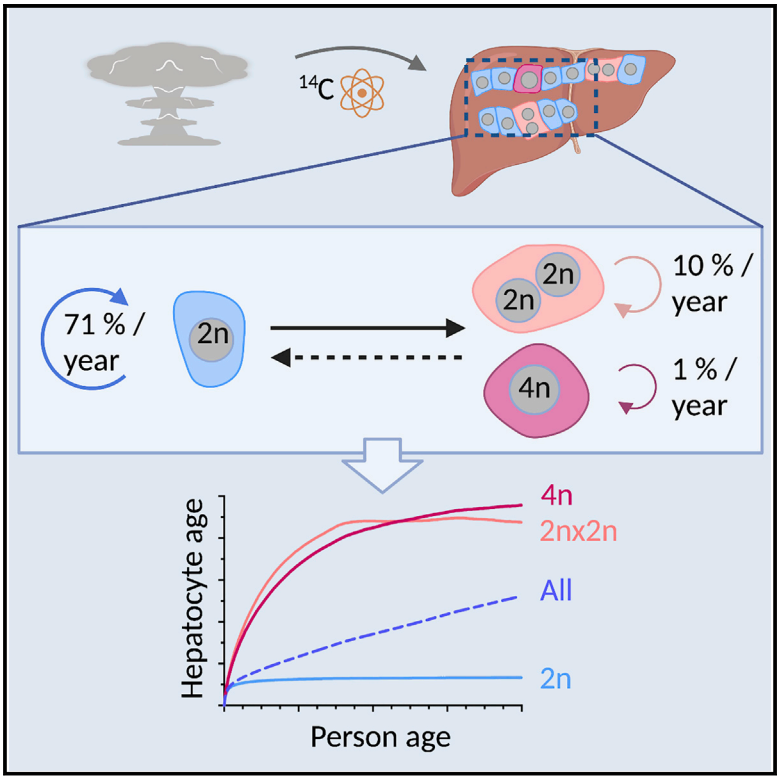

Highlights

- Retrospective ^{14}C birth dating establishes the age of the human liver (<3 years)
- Renewal rates of adult hepatocytes are independent of subject age
- Diploid hepatocytes show more than 7-fold higher birth rates compared with polyploid
- Contribution of higher ploidy levels to the diploid hepatocyte pool is limited

Authors

Paula Heinke, Fabian Rost, Julian Rode, ..., Henrik Druid, Lutz Brusch, Olaf Bergmann

Correspondence

olaf_bergmann@tu-dresden.de

In brief

Based on radiocarbon birth dating, a comprehensive model of hepatocyte renewal in humans shows that the liver remains a young organ. Hepatocytes display a continuous and lifelong turnover, which is highly dependent on their ploidy level.

Heinke et al., 2022, Cell Systems *13*, 499–507
June 15, 2022
https://doi.org/10.1016/j.cels.2022.05.001

CellPress

Cell Systems

CellPress
OPEN ACCESS

Report

Diploid hepatocytes drive physiological liver renewal in adult humans

Paula Heinke,[1] Fabian Rost,[1,2,3] Julian Rode,[3] Palina Trus,[1] Irina Simonova,[1] Enikő Lázár,[4] Joshua Feddema,[1] Thilo Welsch,[5] Kanar Alkass,[6] Mehran Salehpour,[7] Andrea Zimmermann,[8,9] Daniel Seehofer,[8,9] Göran Possnert,[7] Georg Damm,[8,9] Henrik Druid,[6] Lutz Brusch,[3] and Olaf Bergmann[1,4,10,*]

[1]Center for Regenerative Therapies, Technische Universität Dresden, 01307 Dresden, Germany
[2]Max Planck Institute for the Physics of Complex Systems, 01187 Dresden, Germany
[3]Centre for Information Services and High Performance Computing, Technische Universität Dresden, 01187 Dresden, Germany
[4]Department of Cell and Molecular Biology, Karolinska Institutet, 17177 Stockholm, Sweden
[5]Visceral-, Thoracic- and Vascular Surgery, University Hospital Carl Gustav Carus, Technische Universität Dresden, 01307 Dresden, Germany
[6]Department of Oncology-Pathology, Karolinska Institutet, 17177 Stockholm, Sweden
[7]Department of Physics and Astronomy, Applied Nuclear Physics, Ion Physics, Uppsala University, 75120 Uppsala, Sweden
[8]Department of Hepatobiliary Surgery and Visceral Transplantation, University of Leipzig, 04103 Leipzig, Germany
[9]Saxonian Incubator for Clinical Translation (SIKT), Leipzig University, 04103 Leipzig, Germany
[10]Lead contact
*Correspondence: olaf_bergmann@tu-dresden.de
https://doi.org/10.1016/j.cels.2022.05.001

SUMMARY

Physiological liver cell replacement is central to maintaining the organ's high metabolic activity, although its characteristics are difficult to study in humans. Using retrospective radiocarbon (^{14}C) birth dating of cells, we report that human hepatocytes show continuous and lifelong turnover, allowing the liver to remain a young organ (average age <3 years). Hepatocyte renewal is highly dependent on the ploidy level. Diploid hepatocytes show more than 7-fold higher annual birth rates than polyploid hepatocytes. These observations support the view that physiological liver cell renewal in humans is mainly dependent on diploid hepatocytes, whereas polyploid cells are compromised in their ability to divide. Moreover, cellular transitions between diploid and polyploid hepatocytes are limited under homeostatic conditions. With these findings, we present an integrated model of homeostatic liver cell generation in humans that provides fundamental insights into liver cell turnover dynamics.

INTRODUCTION

The liver has a remarkable potential to generate new functional tissue in response to injury, which relies upon the proliferative capacity of liver cells. However, in humans, it remains unknown whether parenchymal hepatocytes are constantly exchanged throughout one's lifetime or whether they are physiologically long-lived cells, similar to cardiomyocytes and neurons (Bergmann et al., 2015; Huttner et al., 2014), that maintain structural and functional integrity over the span of several decades.

During both homeostasis and disease, the replacement of liver parenchyma relies on hepatocytes (Malato et al., 2011; Schaub et al., 2014; Wang et al., 2017; Yanger et al., 2014). The contribution of other cells seems to be only relevant in the cases of severe chronic damage when the normal hepatocyte response is exhausted (Deng et al., 2018; Lu et al., 2015; Raven et al., 2017).

Reports in recent decades, which have relied mainly on cell-cycle markers and nucleotide analogs, have estimated the age of hepatocytes to be between 200 and 400 days in rodents (Macdonald, 1961; Magami et al., 2002). On the other hand, a recent pulse-chase study applying advanced isotope labeling supported the view that within the life span of a mouse, parenchymal liver cells are only rarely exchanged and most are as old as neurons (Arrojo et al., 2019). Estimations of hepatocyte turnover in humans are scarce due to strict methodological limitations. Therefore, it is not known whether the reported hepatocyte renewal paradigm in mice can translate to a human life span of more than 80 years.

Furthermore, it is unclear how pronounced hepatocyte heterogeneity affects cellular turnover. Recent animal studies have provided evidence of distinct subpopulations with special proliferative capacities. Reports have shown that hepatocytes from both the periportal region (Font-Burgada et al., 2015; Pu et al., 2016) and the pericentral region (Wang et al., 2015), as well as midzonal (He et al., 2021; Wei et al., 2021) and randomly distributed hepatocytes (Lin et al., 2018; Planas-Paz et al., 2016) are responsible for maintaining the hepatocyte pool. However, other studies have challenged these findings, and the existence of specific

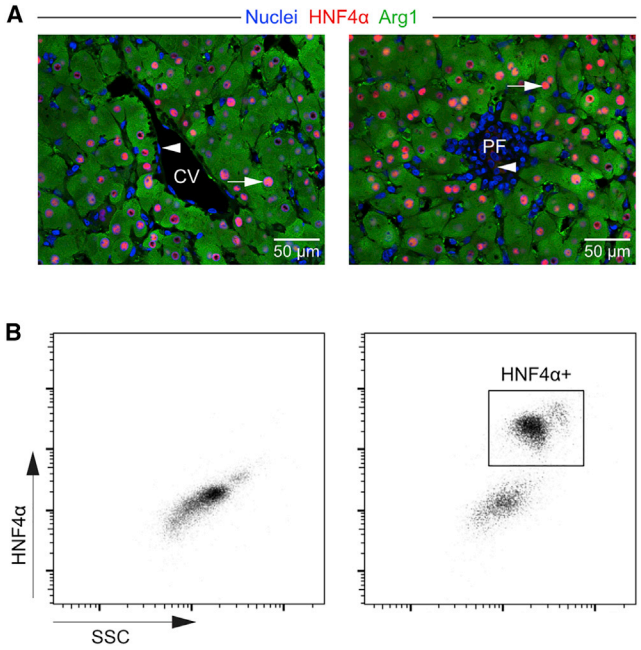

Figure 1. Identification and separation of hepatocyte nuclei in human liver tissue

(A) HNF4α is specifically expressed in all hepatocyte nuclei (arrows) but not in non-hepatocytes (arrowheads) (CV, central vein; PF, portal field), documented by co-labeling with an established cytoplasmic marker for hepatocytes (Arg1). (B) HNF4α immunolabeling (right) can be used to isolate hepatocyte nuclei from non-hepatocyte nuclei using FACS compared with a negative control (left) (representative of n = 35 liver samples). See also Figure S1.

proliferative subpopulations characterized by their zonation has been questioned (Chen et al., 2020; Sun et al., 2020).

In contrast to most other cells in the human body, a fraction of hepatocytes acquire a polyploid state during normal aging (Kudryavtsev et al., 1993). Polyploidy has been attributed to cell-cycle arrest and restricted proliferation in the liver and other tissues (Derks and Bergmann, 2020; Donne et al., 2020; Ganem et al., 2014; Wilkinson et al., 2019). This property has been questioned with regard to hepatocytes based on the results of several mouse studies that have described an equivalent proliferative capacity irrespective of their ploidy level (Duncan et al., 2010; Zhang et al., 2018). Importantly, the evolution and degree of polyploidization show significant interspecies differences. Sixty to seventy percent of human hepatocytes remain diploid over a lifetime (Duncan et al., 2012; Kudryavtsev et al., 1993), whereas up to ninety percent increase their ploidy level in mice (Duncan et al., 2010; Wang et al., 2014). However, the reasons and biological consequences of these variations are poorly understood.

To date, a comprehensive exploration characterizing the dynamics of human hepatocyte turnover, including their age distribution and the consequences for hepatocyte functionality in the aging liver, is lacking. It is important to establish these characteristics of cell renewal in the adult liver, particularly to gain a better understanding of age-related diseases and the development of liver cancer. Here, we provide a comprehensive model of human liver cell turnover and the age distribution of diploid and polyploid hepatocytes through retrospective ^{14}C birth dating and mathematical modeling.

RESULTS

Liver nucleus isolation for retrospective ^{14}C birth dating

Nuclei were isolated from human liver tissue using density gradient centrifugation and incubated with an antibody against the nuclear transcription factor hepatocyte nuclear factor 4 alpha (HNF4α). HNF4α is specifically expressed in hepatocyte nuclei (Si-Tayeb et al., 2010) and therefore enables their identification and separation from non-hepatocyte nuclei isolated from fresh or frozen liver tissue (Figures 1A and 1B). Using fluorescence-activated cell sorting (FACS), we isolated 73.6% ± 10.5% (mean ± SD) hepatocyte nuclei from purified nuclear fractions with no age-related changes (Figures 1B and S1B) in accordance with the known cellular composition of the human liver (Donne et al., 2020). Purities of the sorted HNF4α-positive hepatocyte (98.2% ± 0.9%) and HNF4α-negative non-hepatocyte nuclei populations (97.3% ± 1.5%) were verified by FACS reanalyses (Figure S1A).

Retrospective ^{14}C birth dating of human liver cells

Genomic DNA was extracted from a total of 33 subjects, aged 20–84 (Table S1), from FACS-isolated hepatocyte nuclei (n = 29), non-hepatocyte nuclei (n = 11), and unsorted liver nuclei populations (n = 23) (Table S4). ^{14}C concentrations were determined using accelerator mass spectrometry (Bergmann et al., 2015; Spalding et al., 2013) (Table S2). We corrected ^{14}C concentrations for impurities introduced during nucleus sorting, as described (STAR methods). The comparison of measured ^{14}C values of the samples with historic ^{14}C atmospheric levels, allowed for a first estimate on the magnitude of average genomic ages in hepatic cells (Figures 2A and S2A). Assuming that all cells were generated at the same time, the results indicate a continuous and substantial turnover over the entire lifetime with an average genomic ^{14}C age of 6.1 ± 3.9 years, independent of subject age (Figure S2B). This finding was confirmed by genomic ^{14}C concentrations of sorted hepatocyte nuclei (Figures 2B and 2C) and non-hepatocyte nuclei (Figures S2C and S2D) with average ^{14}C ages of 4.4 ± 4.3 and 8.8 ± 7.0 years, respectively. These results suggest that the human liver is a highly regenerative organ, with most cells being continuously replaced over the human lifespan.

Dynamics of hepatocyte renewal in humans

The measured ^{14}C concentration is a result of the dynamics of cell-cycle activity, which is described by rates of cell birth and cell death (Bergmann et al., 2015; Huttner et al., 2014; Spalding et al., 2013). In cycling cells, DNA is replicated semiconservatively, resulting in daughter cells containing newly formed DNA but also retaining portions of the mother cell's DNA. This leads to a memory effect where the ^{14}C concentration in the daughter cell is an average of the mother cell's ^{14}C concentration and the current atmospheric ^{14}C concentration. In turn, the complete history of cell divisions is needed to predict the ^{14}C concentration for a single cell that makes predictions non-trivial. In contrast to the genomic ^{14}C age described above, which gives only a first estimate of turnover, mathematical models that incorporate the

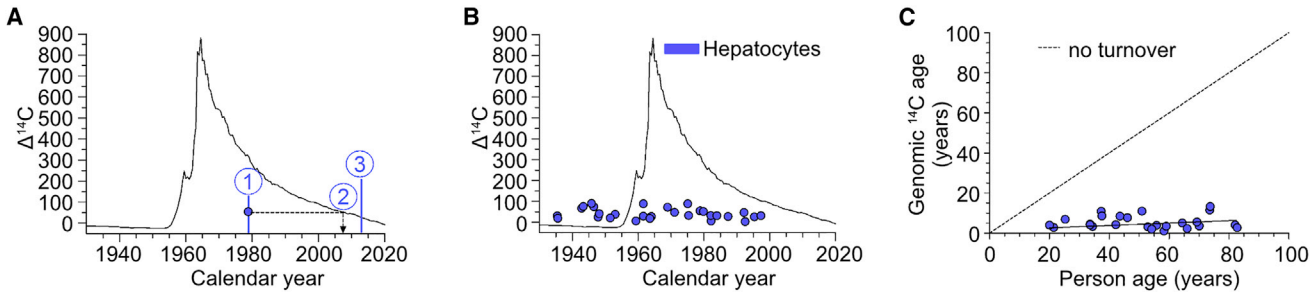

Figure 2. ^{14}C retrospective birth dating of human hepatocytes

(A) Schematic representation of ^{14}C data analysis. Measured ^{14}C data (blue dots) are depicted at the person's birthdate (1). The curve of the equivalent level of the atmospheric ^{14}C (black line) would represent the time point of ^{14}C formation of the analyzed cell population (2, dashed line) if all cells were born at the same time. The difference between the time of sample acquisition (3) and the time point of ^{14}C formation (2) provides an estimate of the genomic ^{14}C age.

(B) Genomic ^{14}C concentrations of hepatocyte nuclei do not correlate with atmospheric ^{14}C concentration at the time of birth.

(C) The estimated ^{14}C age of hepatocyte nuclei is independent of the persons' age, indicating continuous lifelong cellular turnover (linear regression, n = 29, R = 0.26, p = 0.18). See also Figure S2.

dynamics of cell turnover are required to quantitatively characterize the generation of human hepatocytes from our measured genomic ^{14}C data. Hence, we derived a population balance equation for ^{14}C concentration-structured cell populations incorporating a memory effect, which we used to predict the mean ^{14}C concentration dynamics from cell turnover rates (see STAR Methods). We constrained the turnover rates in such a way that the total DNA content of the liver reflects constant nuclei density as well as organ growth over the human life span (Figures S4A–S4C). Applying an additive Gaussian error model (see STAR Methods), we then estimated the cell turnover rates using Bayesian inference. Different population structures and turnover dynamics translate to different model variants, which we termed scenarios. We selected the best-fitting scenario, i.e., the scenario with the highest predictive power, using the leave-one-out (LOO) cross-validation method (Vehtari et al., 2017).

With this approach, we first developed a scenario to analyze the rate at which hepatocytes renew in general, assuming that all cells are replaced at the same frequency. Based on our ^{14}C measurements, this one-population scenario (POP1, Figure S4E) predicts that hepatocytes are dividing at a rate of 19% per year in young age (25 years), with only slight decrease to 17% in middle-aged and old individuals (50–75 years) (Figure S4F), imposed by the change in liver size (Figure S4A; STAR Methods).

Hepatocyte ploidy increases over the lifetime in humans

Rodents develop a considerable amount of hepatocyte binucleation and polyploidy starting around the time of weaning (Guidotti et al., 2003; Margall-Ducos et al., 2007). We described the course of hepatocyte binucleation and polyploidization in adult human liver tissue by automated image analysis of isolated hepatocytes from fresh and frozen liver tissues samples, which we validated by 3D imaging (Figures 3A, S3E, and S3F) and FACS analyses (Figures S3E and S3G). We observed substantial changes in the cellular and nuclear ploidy composition over the lifetime (Figures 3B and S3H). The number of diploid hepatocytes is decreasing with age, in line with previous studies (Kudryavtsev et al., 1993). Although more than 69% of hepatocytes are still diploid in young adults (20–45 years), this fraction drops to less than 58% in old subjects (> 65 years) (Figure 3B). Accordingly, the percentage of polyploid hepatocytes, particularly binucleated diploid and mononucleated tetraploid, increases steadily over the lifetime, reaching up to 40% of all hepatocytes at advanced ages. Higher ploidy classes represent less than 10% of all hepatocytes in adulthood, with less than 5% in young and middle-aged (< 65 years) individuals (Figure S3H).

Ploidy is associated with differences in the age and renewal rates of human hepatocytes

Having analyzed ^{14}C values of hepatocyte nuclei, we went on to separately measure genomic ^{14}C concentrations of primary human hepatocytes (PHH) and hepatocyte nuclei based on different ploidy levels, extending the flow cytometry sorting strategy described above (Figures 3C and 3E). Sorting hepatocyte nuclei allowed a separation based on the nuclear ploidy level (n = 10), where the collected diploid fraction was derived from mononucleated and binucleated diploid hepatocytes, and the polyploid fraction from mononucleated and binucleated polyploid hepatocytes. Cellular ploidy classes were sorted by the cell-based ploidy sorting strategy (n = 4): mononucleated diploid hepatocytes formed the diploid fraction, whereas binucleated diploid cells were part of the polyploid fraction. Reanalyses confirmed the purity of the sorted diploid and polyploid populations (Figures S3I and S3J). Analysis of twelve different paired cases revealed that polyploid hepatocyte nuclei (n = 8, $\Delta\Delta^{14}$C = 14.6 ± 11.3) as well as polyploid hepatocytes (n = 4, $\Delta\Delta^{14}$C = 39.5 ± 20.5) show significantly higher ^{14}C concentrations than diploid from the same individual (Figures 3D and 3F). The ^{14}C concentrations of polyploid populations correspond to time points before the ^{14}C formation date of diploid populations, suggesting that polyploid hepatocytes are older than diploid hepatocytes and might have different turnover characteristics (Figure 2A).

Consequently, we developed two more refined mathematical scenarios (scenario POP2p and POP3p) to fit all measured ^{14}C data from total hepatocyte nuclear fractions, ploidy-sorted hepatocyte nuclei, and ploidy-sorted hepatocytes. These scenarios describe diploid and polyploid hepatocyte populations with distinct rates of cell division and cell death (Figures 4A and S4E; STAR Methods) and account for ploidy exchanges

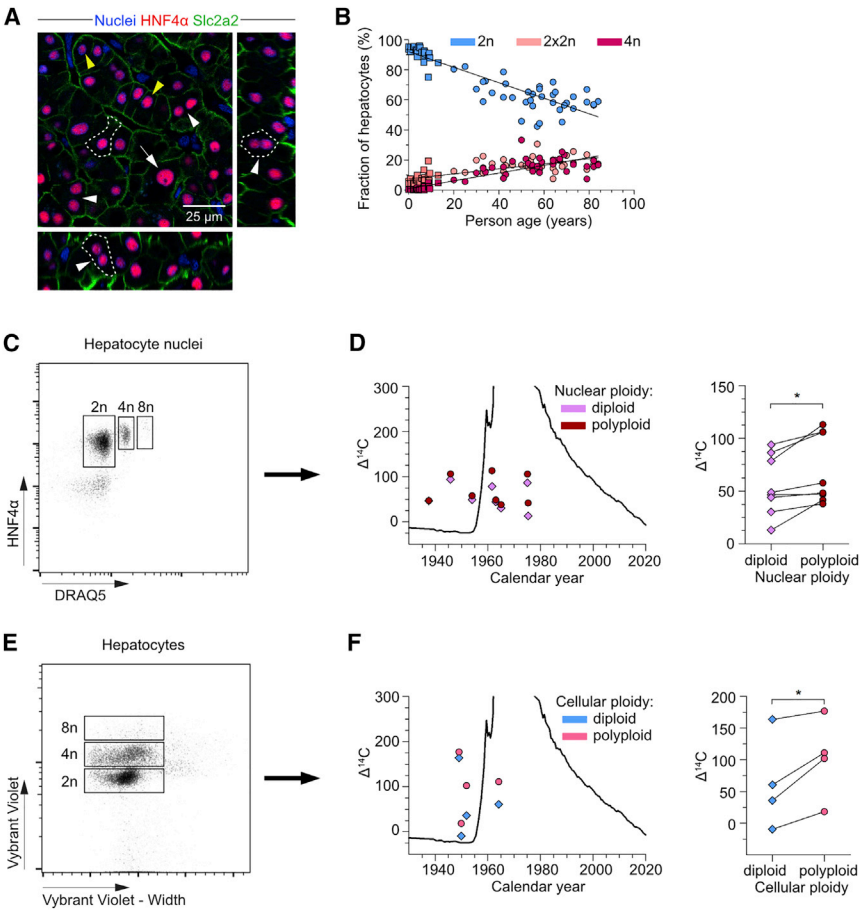

Figure 3. The human liver is composed of polyploid hepatocytes with different genomic ^{14}C ages

(A) Human hepatocytes exhibit cellular and nuclear ploidy (yellow arrowheads = mononucleated diploid, white arrowheads = binucleated diploid, white arrow = mononucleated polyploid, dashed lines label the same hepatocyte in the three stereological views).

(B) Automated image analysis of isolated hepatocytes (circles) was applied to develop hepatocyte ploidy profiles. Pediatric ploidy data are taken from Gahan and Middleton (1984) (squares). The analysis shows an age-dependent decrease of mononucleated diploid hepatocytes (linear regression, n = 62, R = 0.89, $p < 0.0001$) and increase of binucleated diploid (linear regression, n = 62, R = 0.75, $p < 0.0001$) and mononucleated tetraploid hepatocytes (linear regression, n = 62, R = 0.86, $p < 0.0001$).

(C) Separation of diploid (2n) and polyploid (pn) hepatocyte nuclei with DNA stain (DRAQ5) using FACS (representative of n = 10 liver samples).

(D) Polyploid hepatocyte nuclei show higher genomic ^{14}C levels than diploid nuclei (paired t test, n = 8, *p = 0.01).

(E) Separation of diploid (2n) and polyploid hepatocytes (2x2n and pn) with DNA stain (Vybrant violet) using FACS (representative of n = 4 primary human hepatocyte samples).

(F) Polyploid hepatocytes show higher genomic ^{14}C levels than diploid (paired t test, n = 4, *p = 0.04). See also Figure S3.

between the ploidy classes. To allow more precise parameter estimates and because most polyploid hepatocytes are tetraploid (Figures 3B and S3H), we neglected higher ploidy levels (see STAR Methods). By considering the ploidy composition of the hepatocytes (Figure 3B), these scenarios allow us to predict ^{14}C concentrations for the three different hepatocyte sorts: total hepatocyte nuclear fractions, ploidy-sorted hepatocyte nuclei, and ploidy-sorted hepatocytes. In turn, by exploiting the different compositions of the three sorting strategies, we were able to estimate turnover rates for each individual hepatocyte ploidy class. Compared with the POP2p scenario, the more complex POP3p scenario subdivided the polyploid population into a binucleated diploid and a mononucleated tetraploid population (Figure S4E). We constrained the turnover rates such that the scenarios correctly predicted the changes in the composition of ploidy populations during adulthood (Figure 4; STAR Methods).

In both scenarios POP2p and POP3p, the renewal dynamics of diploid and polyploid hepatocytes showed no considerable age-related changes during adulthood, in line with the above-tested scenario POP1 (Figures 4B, S4F, and S4G). However, diploid and polyploid hepatocyte populations display very different turnover characteristics. In a middle-aged individual, the annual cell division rate for diploid hepatocytes is approximately 71%, whereas it is only 10% among binucleated diploid and 1% among mononucleated tetraploid hepatocytes (POP3p, Figure 4B). This corresponds to average cell ages of 0.7 years for diploid hepatocytes, and 4.4 years for both binucleated diploid hepatocytes and mononucleated tetraploid hepatocytes (Figure 4C). Given a total hepatocyte number of 2.5×10^{11} in a human middle-aged liver (Figure S4D), we estimate that approximately 700 million hepatocytes are born every day (see STAR Methods).

Although 95% of all diploid cells are exchanged within a year, up to 12% of polyploid cells reside more than one decade in the organ (POP3p, Figure 4D). As the fraction of polyploid hepatocytes increases over the lifetime, the age distribution of hepatocytes changes accordingly in aging individuals (POP3p, Figures 4D–4F). In a 25-year-old individual, 84% of hepatocytes are less than 2 years old, whereas this fraction decreases to 67% in a 75-year-old subject. Although polyploid hepatocytes live substantially longer than diploid hepatocytes, most liver cells are short lived, irrespective of age, and more than half of all hepatocytes have been born within the last year.

The ploidy conveyor in human liver

The ploidy turnover scenarios not only estimate the dynamics of hepatocyte generation for diploid and polyploid cells but also describes cellular transitions between ploidy classes, as previously suggested with the concept of a ploidy conveyor (Duncan et al., 2010) (Figure S4E). Due to reduced complexity of the POP2p scenario, the bidirectional exchange rates between hepatocyte populations become strictly identifiable to explain the measured ^{14}C age distributions (see STAR Methods). In a 25-year-old

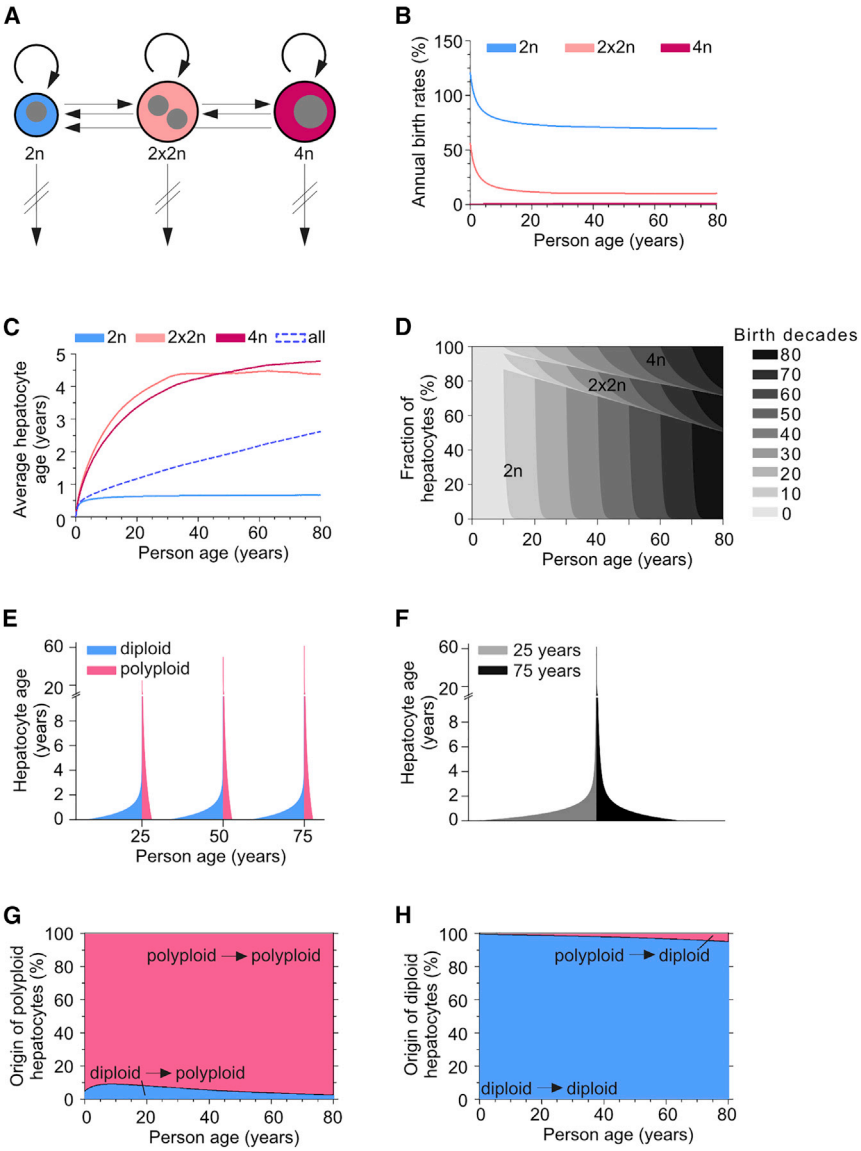

Figure 4. Ploidy is associated with the renewal dynamics and age distribution of human hepatocytes

(A) The mathematical scenario POP3p with the best fit to our measured genomic ^{14}C levels describes cellular birth (circular arrows) and death rates (downwards arrows) of mononucleated diploid (2n), binucleated diploid (2x2n), and mononucleated tetraploid (4n) hepatocytes, and an exchange between the ploidy classes (horizontal arrows).

(B) Estimated annual birth rates of 2n, 2x2n, and 4n hepatocytes remain nearly constant during adulthood (POP3p).

(C) The average cellular age of polyploid hepatocytes is more than 6-fold higher than that of diploid hepatocytes. Because polyploidization advances with age, the overall hepatocyte age increases (POP3p).

(D) The age distribution of human hepatocytes is illustrated for a person's given age (POP3p). The decade in which a cell was born is shown in different shades of gray. Polyploid hepatocytes remain in the liver much longer than diploid hepatocytes.

(E) Age distribution of diploid and polyploid (2x2n + 4n) hepatocytes at 25, 50, and 75 years of age (POP3p). The average cellular age as well as the fraction of polyploid cells increases within the lifetime.

(F) Comparative age distribution of all hepatocytes at 25 and 75 years of age illustrates the accumulation of older cells over the lifetime (POP3p).

(G) There is a lifelong contribution of diploid hepatocytes to the polyploid cell pool (POP2p). However, the majority of polyploid hepatocytes arise from cells of the same ploidy class by cell division.

(H) Most diploid hepatocytes originate from the pool of diploid hepatocytes, and only a small fraction derives from the polyploid hepatocyte pool by ploidy reversal (POP2p). See also Figure S4.

subject, approximately 7% of polyploid hepatocytes arise from diploid cells (POP2p, Figure 4G). Due to the continuous increase in ploidy level, this exchange rate drops to 3% in a 75-year-old individual. In contrast, only 1% of the diploid population originates from polyploid hepatocytes at a young age, and 4% of diploid hepatocytes are generated by the polyploid hepatocyte pool in old individuals (POP2p, Figure 4H). However, the vast majority of diploid and polyploid hepatocytes are maintained through renewal processes within their individual ploidy class (Figures 4G and 4H).

DISCUSSION

Our current understanding of human liver homeostasis is far from complete, and we have limited knowledge regarding to what degree the replacement of parenchymal cells is required to maintain the high metabolic activity of hepatocytes. Here, we used ^{14}C retrospective birth dating to evaluate the birth rates and turnover dynamics of human liver cells. We found fundamental differences in the renewal between diploid and polyploid hepatocytes: diploid cells are exchanged approximately once a year, although higher ploidy classes reside up to one decade in the organ.

The human liver remains a young organ

It is generally agreed that hepatocytes retain their ability to renew in adulthood under physiological conditions (Macdonald, 1961). A clear picture of the renewal behavior of parenchymal liver cells in humans has been lacking until now. The turnover rate of adult hepatocytes has been studied in a number of animal models (Arrojo et al., 2019; Magami et al., 2002), but it remains unknown whether these results can be translated to humans. A recent study using ^{15}N labeling showed that the majority of murine hepatocytes are not replaced within the observational period of 18 months (Arrojo et al., 2019). The authors concluded that most hepatocytes are not exchanged and are as old as post-mitotic neurons. However, in humans, 1.5 years represent a rather short episode in life, and much longer observation periods are necessary to conclude that most hepatocytes do not renew in a lifetime. Studies in

humans, which are based on the expression of the cell-cycle marker Ki-67, have revealed a very low labeling index in homeostasis (< 0.5%) (Vansaun et al., 2013) (Figure S1C). However, such imaging approaches reflect cell-cycle activity only at a single time point without knowing the fate of the cycling cell. Moreover, they do not provide information as to whether there are subpopulations of hepatocytes that show different cycling frequencies. Thus, these studies based on the detection of cell-cycle markers are insufficient to establish reliable turnover rates in humans (Spalding et al., 2008).

In contrast, ^{14}C birth dating provides a cumulative measure of cell renewal, which makes it possible to retrospectively study cellular turnover in human tissue samples (Spalding et al., 2005). ^{14}C birth dating has been applied to many organs to characterize cellular ages and turnover dynamics (Bergmann et al., 2009; Spalding et al., 2013; Yeung et al., 2019). These studies have shown that ^{14}C levels in genomic DNA accurately represent atmospheric ^{14}C concentrations from the time point of cell generation. Exchange of carbon atoms in genomic DNA at later time points, such as methylation and DNA repair, does not affect the measured ^{14}C levels (Figure S5A) (Spalding et al., 2005). Even a 100-fold higher level of DNA repair compared with cortical neurons would affect the estimated annual birth rate only by 0.3% (Figure S5B). Recently, independent laboratories using next-generation sequencing observed low amounts (< 5%) of aneuploidy and copy-number variations in hepatocytes (Knouse et al., 2014; Sladky et al., 2020). These studies suggest that the genomic stability of hepatocytes is similar to that of neurons (Knouse et al., 2014) and therefore would not affect the results of ^{14}C retrospective birth dating (Bergmann et al., 2012; Huttner et al., 2014).

We applied retrospective ^{14}C birth dating to explore cell turnover in the human liver. By analyzing unsorted liver nuclei, we report an average liver cell age of less than three years using the simplified one-population scenario POP1. This finding provides a first indication that the human liver remains a young organ and constantly renews throughout a person's lifetime.

As the organ comprises different cell types, we further separated nuclei from hepatocytes and non-hepatocytes. Genomic ^{14}C concentrations suggest that hepatocytes are renewed over the whole human lifetime, with a birth rate of 19% per year and an average age of 2.7 years in young individuals. This turnover is slightly higher than the renewal in medium and high age (17% per year, average hepatocyte age 2.9 years), which coincides with the continuous growth of the liver organ up to a middle age (Choukèr et al., 2004) (Figure S4A). Non-hepatocytes are only a small fraction of liver cells but represent a very diverse group with various functions. The largest populations include endothelial, Kupffer, and stellate cells. However, a real characterization of their unique renewal dynamics is missing. Our obtained ^{14}C data provide general insight into the turnover behavior of non-hepatocytes. We determined an average birth rate decreasing with age from 16% in young individuals (25 years) to 13% at 75 years of age. However, as we did not focus on characterizing the renewal rates of individual subpopulations, our ^{14}C measurements provide only an estimate of the average turnover rate of all non-hepatocytes.

Hepatocyte ploidy determines cellular renewal capacity

Polyploidy has been described in several organs of the body, including the heart (Bergmann et al., 2015) and the liver (Bou-Nader et al., 2020). However, the nature and biological role of ploidy is only poorly understood (Derks and Bergmann, 2020). In contrast to other organs, polyploidy in the liver does not contradict proliferation or regeneration in animal studies (Lin et al., 2020; Zhang et al., 2018). In humans, there is little knowledge on how polyploid cells, which represent a much lower fraction than in the murine organ, contribute to tissue renewal.

We show that human polyploid hepatocytes maintain their ability to renew. However, the chance to be renewed is more than 7-fold lower than that of diploid cells. Polyploid hepatocytes can remain in the liver for more than a decade, forming a subpopulation of long-lived cells. This apparent proliferative advantage of diploid over polyploid hepatocytes is supported by numerous publications (Chen et al., 2020; Wang et al., 2015; Wilkinson et al., 2019). However, in contrast to humans, most murine hepatocytes (90%) become polyploid starting approximately at the time of weaning (Duncan et al., 2010; Wang et al., 2014). A recent mouse study labeling all preexisting cells with ^{15}N showed that 95% of all hepatocytes are not replaced within 1.5 years (Arrojo et al., 2019), indicating that most hepatocytes are long lived. Whether the described small fraction of renewing murine hepatocytes might correspond to diploid hepatocytes with a higher turnover rate, as we report in humans, remains an open question and requires further investigation.

In mice, the distribution of polyploidy is strongly related to zonal localization (Matsumoto et al., 2020; Morales-Navarrete et al., 2015; Tanami et al., 2017). Therefore, it seems possible that different renewal capacities of the ploidy classes also reflect hepatocyte zonation. However, in the human liver, no particular ploidy distribution regarding liver zonation has been reported (Bou-Nader et al., 2020), indicating that renewal of hepatocytes may not be related to zonal assignment. This difference underlines that the age distribution of hepatocytes varies across species and that cell renewal in the mouse liver is different from that in humans.

The polyploid hepatocyte population is mainly maintained by self-renewal

The increase in hepatocyte ploidy over the lifetime was described several decades ago (Kudryavtsev et al., 1993). However, there are few data on the mechanism of this ploidy change in the human liver. Aberrant cell-cycle activity of diploid hepatocytes has been seen as the main driver of polyploidy in the liver (Celton-Morizur et al., 2009; Margall-Ducos et al., 2007). Therefore, we were interested in understanding how often aberrant cell-cycle activity results in a change in ploidy class in humans. We observed that, independent of subject age, almost all diploid hepatocytes showed regular cell divisions (>99%). At the same time, dependent on age, approximately 21%–24% of polyploid cells entering the cell cycle return to diploidy during adulthood. The fractions of human hepatocytes changing the ploidy level are in the same range as in murine models (Duncan et al., 2010).

We observed that an increase in the ploidy level is necessary to explain the initial generation of polyploid liver cells. However, the significant difference between the ^{14}C concentrations in diploid and polyploid hepatocyte nuclei (Figures 3D and 3F) already indicates that such ploidy transition processes play only a minor role. The more refined analysis with our mathematical model confirms

that the exchange between the diploid and polyploid population is several-fold lower than the individual renewal rates of diploid and polyploid hepatocytes (birth and death of cells). We report that in young individuals, approximately 7% of polyploid hepatocytes originate from diploid hepatocytes, whereas this fraction drops to 3% in older individuals (Figure 4G). Thus, the majority of polyploid cells do not arise by a ploidy increase from diploid cells but due to proliferation of already existing polyploid hepatocytes. In the last decade, the importance of a bidirectional exchange between different ploidy levels for maintaining liver homeostasis has been emphasized in the ploidy conveyor model (Duncan et al., 2010), although a more recent publication suggests that the murine polyploid cell compartment remains stable over 18 months in homeostasis (Matsumoto et al., 2020). We observed that the contribution of polyploid cells to the diploid cell pool was less than 4% over the whole lifetime (Figure 4H), playing only a minor role in cell generation. In conclusion, our model implies that the age-related increase in human hepatocyte polyploidy is mainly attributed to a net increase in newly generated cells within the individual polyploid hepatocyte pool.

Continuous renewal of hepatocytes in the aging liver

It is important to understand the impact of aging on cell renewal in the human liver, as many chronic liver diseases show a higher prevalence in aged individuals (Kim et al., 2015). Until now, there have been only limited data available on age-dependent hepatocellular renewal (Macdonald, 1961) and its impact on liver function. Our model provides no evidence that the renewal rates of adult hepatocytes are affected by the subject's age, with almost constant birth rates in diploid and polyploid hepatocytes, respectively (Figure 4B). However, due to the relative increase in the size of the polyploid compartment in the aging liver, the average hepatocyte age, and their age distribution change over the human lifespan (Figures 4C–4F).

Polyploid cells have been associated with aneuploidy and genomic instability (Storchova and Pellman, 2004). However, we found substantially lower turnover rates in polyploid hepatocytes, possibly being a protective mechanism against replicative senescence and somatic mutations. Moreover, polyploidy has been suggested to be an adaptive response forming a buffer against oxidative stress and DNA damage, increasing in liver aging and disease processes (Gentric and Desdouets, 2014).

Although our model is based on the assumption that hepatocytes are self-renewing cells, we cannot exclude that other cells contribute to the pool of new hepatocytes as suggested under pathological conditions (Deng et al., 2018; Lu et al., 2015; Raven et al., 2017). Extending our POP2p scenario (POP2p_stem, Figure S4E, STAR Methods), we showed that a putative contribution of a stem-cell-like population to the diploid hepatocyte pool has to be small (0.04% per year in a middle-aged individual). It results in similar renewal rates of diploid and polyploid hepatocytes as described by the scenarios POP2p and POP3p (STAR Methods), strengthening the robustness of the cell turnover rates presented here.

In summary, ^{14}C retrospective birth dating revealed that the human liver remains a young organ even in elderly individuals. Over the whole lifetime, we observed a constant and high turnover of hepatocytes that is strongly associated with ploidy level. Exchange between the ploidy classes plays only a minimal role in liver homeostasis in humans. Whether long-lived polyploid cells make the liver more susceptible to age-dependent diseases or act as a resilience factor to cope with cellular stress, thereby preventing loss of organ function and cancer, remains an important question to be addressed.

STAR★METHODS

Detailed methods are provided in the online version of this paper and include the following:

- KEY RESOURCES TABLE
- RESOURCE AVAILABILITY
  - Lead contact
  - Materials availability
  - Data and code availability
- EXPERIMENTAL MODEL AND SUBJECT DETAILS
- METHOD DETAILS
  - Isolation and cryopreservation of PHH
  - Nucleus isolation
  - Flow cytometry analysis and sorting
  - DNA extraction from nuclei
  - DNA extraction from PHH
  - Accelerator mass spectrometry (AMS)
  - Immunohistochemistry (IHC)
  - Cell isolation from liver tissue and immunolabeling
  - Automated determination of ploidy distribution
  - 3D image analysis of hepatocyte ploidy
  - Analysis of hepatocyte DNA density
  - Analysis of human liver size
  - Mathematical modeling of ^{14}C dynamics
- QUANTIFICATION AND STATISTICAL ANALYSIS

SUPPLEMENTAL INFORMATION

Supplemental information can be found online at https://doi.org/10.1016/j.cels.2022.05.001.

ACKNOWLEDGMENTS

We thank Magdalena Kretschmer for technical assistance and Steffen Rulands and Fabrizio Olmeda for advice on mathematical modeling. This work was supported by the Flow Cytometry Facility, the Light Microscopy Facility and Histology Facility, all Core Facilities of the CMCB Technology Platform at TU Dresden. O.B. was supported by the Center for Regenerative Therapies Dresden, the Karolinska Institutet, the Swedish Research Council, the Ragnar Söderberg Foundation, the Åke Wiberg Foundation, and the LeDucq foundation. L.B. acknowledges support by the BMBF (grants 031L0033 and 031L0258A). The model simulations and Bayesian inference were performed on HPC resources granted by the ZIH at TU Dresden. The graphical abstract was created with BioRender.com.

AUTHOR CONTRIBUTIONS

Conceptualization, P.H. and O.B.; methodology, P.H., F.R., J.R., M.S., G.D., L.B., and O.B.; software, F.R., J.R., and L.B.; investigation, P.H., P.T., I.S., E.L., J.F., A.Z., G.D., and O.B.; resources, T.W., K.A., H.D., D.S., and G.D.; writing – original draft, P.H., F.R., J.R., E.L., G.D., and O.B.; writing – review & editing, P.H., F.R., J.R., E.L., G.D., and O.B.; supervision, M.S., G.P., G.D., H.D., L.B., and O.B.; funding acquisition, L.B. and O.B.

DECLARATION OF INTERESTS

The authors declare no competing interests.

Received: August 13, 2020
Revised: February 19, 2022
Accepted: May 9, 2022
Published: May 31, 2022

REFERENCES

Bergmann, O., Bhardwaj, R.D., Bernard, S., Zdunek, S., Barnabé-Heider, F., Walsh, S., Zupicich, J., Alkass, K., Buchholz, B.A., Druid, H., et al. (2009). Evidence for cardiomyocyte renewal in humans. Science *324*, 98–102.

Bergmann, O., Liebl, J., Bernard, S., Alkass, K., Yeung, M.S., Steier, P., Kutschera, W., Johnson, L., Landén, M., Druid, H., et al. (2012). The age of olfactory bulb neurons in humans. Neuron *74*, 634–639.

Bergmann, O., Zdunek, S., Felker, A., Salehpour, M., Alkass, K., Bernard, S., Sjostrom, S.L., Szewczykowska, M., Jackowska, T., dos Remedios, C., et al. (2015). Dynamics of cell generation and turnover in the human heart. Cell *161*, 1566–1575.

Bernard, S., Frisén, J., and Spalding, K.L. (2010). A mathematical model for the interpretation of nuclear bomb test derived 14C incorporation in biological systems. Nucl. Instrum. Methods Phys. Res. B *268*, 1295–1298.

Bhardwaj, R.D., Curtis, M.A., Spalding, K.L., Buchholz, B.A., Fink, D., Björk-Eriksson, T., Nordborg, C., Gage, F.H., Druid, H., Eriksson, P.S., and Frisén, J. (2006). Neocortical neurogenesis in humans is restricted to development. Proc. Natl. Acad. Sci. USA *103*, 12564–12568.

Bou-Nader, M., Caruso, S., Donne, R., Celton-Morizur, S., Calderaro, J., Gentric, G., Cadoux, M., L'Hermitte, A., Klein, C., Guilbert, T., et al. (2020). Polyploidy spectrum: a new marker in HCC classification. Gut *69*, 355–364.

Celton-Morizur, S., Merlen, G., Couton, D., Margall-Ducos, G., and Desdouets, C. (2009). The insulin/Akt pathway controls a specific cell division program that leads to generation of binucleated tetraploid liver cells in rodents. J. Clin. Invest. *119*, 1880–1887.

Chen, F., Jimenez, R.J., Sharma, K., Luu, H.Y., Hsu, B.Y., Ravindranathan, A., Stohr, B.A., and Willenbring, H. (2020). Broad distribution of hepatocyte proliferation in liver homeostasis and regeneration. Cell Stem Cell *26*, 27–33.e4.

Choukèr, A., Martignoni, A., Dugas, M., Eisenmenger, W., Schauer, R., Kaufmann, I., Schelling, G., Löhe, F., Jauch, K.W., Peter, K., and Thiel, M. (2004). Estimation of liver size for liver transplantation: the impact of age and gender. Liver Transpl. *10*, 678–685.

Damm, G., Schicht, G., Zimmermann, A., Rennert, C., Fischer, N., Kießig, M., Wagner, T., Kegel, V., and Seehofer, D. (2019). Effect of glucose and insulin supplementation on the isolation of primary human hepatocytes. Excli J. *18*, 1071–1091.

Deng, X., Zhang, X., Li, W., Feng, R.X., Li, L., Yi, G.R., Zhang, X.N., Yin, C., Yu, H.Y., Zhang, J.P., et al. (2018). Chronic liver injury induces conversion of biliary epithelial cells into hepatocytes. Cell Stem Cell *23*, 114–122.e3.

Derks, W., and Bergmann, O. (2020). Polyploidy in cardiomyocytes: roadblock to heart regeneration? Circ. Res. *126*, 552–565.

Donne, R., Saroul-Aïnama, M., Cordier, P., Celton-Morizur, S., and Desdouets, C. (2020). Polyploidy in liver development, homeostasis and disease. Nat. Rev. Gastroenterol. Hepatol. *17*, 391–405.

Duncan, A.W., Hanlon Newell, A.E., Smith, L., Wilson, E.M., Olson, S.B., Thayer, M.J., Strom, S.C., and Grompe, M. (2012). Frequent aneuploidy among normal human hepatocytes. Gastroenterology *142*, 25–28.

Duncan, A.W., Taylor, M.H., Hickey, R.D., Hanlon Newell, A.E., Lenzi, M.L., Olson, S.B., Finegold, M.J., and Grompe, M. (2010). The ploidy conveyor of mature hepatocytes as a source of genetic variation. Nature *467*, 707–710.

Arrojo e Drigo, R., Lev-Ram, V., Tyagi, S., Ramachandra, R., Deerinck, T., Bushong, E., Phan, S., Orphan, V., Lechene, C., Ellisman, M.H., and Hetzer, M.W. (2019). Age mosaicism across multiple scales in adult tissues. Cell Metab. *30*, 343–351.e343.

Font-Burgada, J., Shalapour, S., Ramaswamy, S., Hsueh, B., Rossell, D., Umemura, A., Taniguchi, K., Nakagawa, H., Valasek, M.A., Ye, L., et al. (2015). Hybrid periportal hepatocytes regenerate the injured liver without giving rise to Cancer. Cell *162*, 766–779.

Foreman-Mackey, D., Hogg, D.W., Lang, D., and Goodman, J. (2013). Emcee: the MCMC Hammer. Publ. Astron. Soc. Pac. *125*, 306–312.

Fröhlich, F., Kaltenbacher, B., Theis, F.J., and Hasenauer, J. (2017). Scalable parameter estimation for genome-scale biochemical reaction networks. PLoS Comput. Biol. *13*, e1005331.

Gahan, P.B., and Middleton, J. (1984). Euploidization of human hepatocytes from donors of different ages and both sexes compared with those from cases of Werner's syndrome and progeria. Exp. Gerontol. *19*, 355–358.

Ganem, N.J., Cornils, H., Chiu, S.Y., O'Rourke, K.P., Arnaud, J., Yimlamai, D., Théry, M., Camargo, F.D., and Pellman, D. (2014). Cytokinesis failure triggers hippo tumor suppressor pathway activation. Cell *158*, 833–848.

Gentric, G., and Desdouets, C. (2014). Polyploidization in liver tissue. Am. J. Pathol. *184*, 322–331.

Georgiadou, E., Stenström, K.E., Uvo, C.B., Nilsson, P., Skog, G., and Mattsson, S. (2013). Bomb-pulse 14C analysis combined with 13C and 15-N measurements in blood serum from residents of Malmö, Sweden. Radiat. Environ. Biophys. *52*, 175–187.

Guidotti, J.E., Brégerie, O., Robert, A., Debey, P., Brechot, C., and Desdouets, C. (2003). Liver cell polyploidization: a pivotal role for binuclear hepatocytes. J. Biol. Chem. *278*, 19095–19101.

Hasenauer, J., Schittler, D., and Allgöwer, F. (2012). Analysis and simulation of division- and label-structured population models: a new tool to analyze proliferation assays. Bull. Math. Biol. *74*, 2692–2732.

He, L., Pu, W., Liu, X., Zhang, Z., Han, M., Li, Y., Huang, X., Han, X., Li, Y., Liu, K., et al. (2021). Proliferation tracing reveals regional hepatocyte generation in liver homeostasis and repair. Science *371*, eabc4346.

Heinemann, A., Wischhusen, F., Püschel, K., and Rogiers, X. (1999). Standard liver volume in the Caucasian population. Liver Transpl. Surg. *5*, 366–368.

Hross, S., and Hasenauer, J. (2016). Analysis of CFSE time-series data using division-, age- and label-structured population models. Bioinformatics *32*, 2321–2329.

Huttner, H.B., Bergmann, O., Salehpour, M., El Cheikh, R., Nakamura, M., Tortora, A., Heinke, P., Coras, R., Englund, E., Eyüpoglu, I.Y., et al. (2018). Meningioma growth dynamics assessed by radiocarbon retrospective birth dating. EBiomedicine *27*, 176–181.

Huttner, H.B., Bergmann, O., Salehpour, M., Rácz, A., Tatarishvili, J., Lindgren, E., Csonka, T., Csiba, L., Hortobágyi, T., Méhes, G., et al. (2014). The age and genomic integrity of neurons after cortical stroke in humans. Nat. Neurosci. *17*, 801–803.

Johnson, T.N., Tucker, G.T., Tanner, M.S., and Rostami-Hodjegan, A. (2005). Changes in liver volume from birth to adulthood: a meta-analysis. Liver Transpl. *11*, 1481–1493.

Kegel, V., Deharde, D., Pfeiffer, E., Zeilinger, K., Seehofer, D., and Damm, G. (2016). Protocol for isolation of primary human hepatocytes and corresponding major populations of non-parenchymal liver cells. J. Vis. Exp. e53069.

Kim, I.H., Kisseleva, T., and Brenner, D.A. (2015). Aging and liver disease. Curr. Opin. Gastroenterol. *31*, 184–191.

Knouse, K.A., Wu, J., Whittaker, C.A., and Amon, A. (2014). Single cell sequencing reveals low levels of aneuploidy across mammalian tissues. Proc. Natl. Acad. Sci. USA *111*, 13409–13414.

Kudryavtsev, B.N., Kudryavtseva, M.V., Sakuta, G.A., and Stein, G.I. (1993). Human hepatocyte polyploidization kinetics in the course of life cycle. Virchows Arch. B Cell Pathol. Incl. Mol. Pathol. *64*, 387–393.

Lin, S., Nascimento, E.M., Gajera, C.R., Chen, L., Neuhöfer, P., Garbuzov, A., Wang, S., and Artandi, S.E. (2018). Distributed hepatocytes expressing telomerase repopulate the liver in homeostasis and injury. Nature *556*, 244–248.

Lin, Y.H., Zhang, S., Zhu, M., Lu, T., Chen, K., Wen, Z., Wang, S., Xiao, G., Luo, D., Jia, Y., et al. (2020). Mice With increased numbers of polyploid hepatocytes maintain regenerative capacity but develop fewer hepatocellular carcinomas following chronic liver injury. Gastroenterology *158*, 1698–1712.e14.

Liu, H., Bersell, K., and Kühn, B. (2021). Isolation and characterization of intact cardiomyocytes from frozen and fresh human myocardium and mouse hearts. Methods Mol. Biol. *2158*, 199–210.

Lu, W.Y., Bird, T.G., Boulter, L., Tsuchiya, A., Cole, A.M., Hay, T., Guest, R.V., Wojtacha, D., Man, T.Y., Mackinnon, A., et al. (2015). Hepatic progenitor cells of biliary origin with liver repopulation capacity. Nat. Cell Biol. *17*, 971–983.

Macdonald, R.A. (1961). "Lifespan" of liver cells. Autoradio-graphic study using tritiated thymidine in normal, cirrhotic, and partially hepatectomized rats. Arch. Intern. Med. *107*, 335–343.

Magami, Y., Azuma, T., Inokuchi, H., Kokuno, S., Moriyasu, F., Kawai, K., and Hattori, T. (2002). Cell proliferation and renewal of normal hepatocytes and bile duct cells in adult mouse liver. Liver *22*, 419–425.

Malato, Y., Naqvi, S., Schürmann, N., Ng, R., Wang, B., Zape, J., Kay, M.A., Grimm, D., and Willenbring, H. (2011). Fate tracing of mature hepatocytes in mouse liver homeostasis and regeneration. J. Clin. Invest. *121*, 4850–4860.

Margall-Ducos, G., Celton-Morizur, S., Couton, D., Brégerie, O., and Desdouets, C. (2007). Liver tetraploidization is controlled by a new process of incomplete cytokinesis. J. Cell Sci. *120*, 3633–3639.

Matsumoto, T., Wakefield, L., Tarlow, B.D., and Grompe, M. (2020). In vivo lineage tracing of polyploid hepatocytes reveals extensive proliferation during liver regeneration. Cell Stem Cell *26*, 34–47.e3.

Morales-Navarrete, H., Segovia-Miranda, F., Klukowski, P., Meyer, K., Nonaka, H., Marsico, G., Chernykh, M., Kalaidzidis, A., Zerial, M., and Kalaidzidis, Y. (2015). A versatile pipeline for the multi-scale digital reconstruction and quantitative analysis of 3D tissue architecture. eLife *4*.

Nagy, P., Thorgeirsson, S.S., and Grisham, J.W. (2020). Organizational principles of the liver. In the liver, I.M. Arias, H.J. Alter, J.L. Boyer, D.E. Cohen, D.A. Shafritz, S.S. Thorgeirsson, and A.W. Wolkoff, eds., pp. 1–13.

Planas-Paz, L., Orsini, V., Boulter, L., Calabrese, D., Pikiolek, M., Nigsch, F., Xie, Y., Roma, G., Donovan, A., Marti, P., et al. (2016). The RSPO–LGR4/5–ZNRF3/RNF43 module controls liver zonation and size. Nat. Cell Biol. *18*, 467–479.

Pu, W., Zhang, H., Huang, X., Tian, X., He, L., Wang, Y., Zhang, L., Liu, Q., Li, Y., Li, Y., et al. (2016). Mfsd2a+ hepatocytes repopulate the liver during injury and regeneration. Nat. Commun. *7*, 13369.

Raven, A., Lu, W.Y., Man, T.Y., Ferreira-Gonzalez, S., O'Duibhir, E., Dwyer, B.J., Thomson, J.P., Meehan, R.R., Bogorad, R., Koteliansky, V., et al. (2017). Cholangiocytes act as facultative liver stem cells during impaired hepatocyte regeneration. Nature *547*, 350–354.

Réu, P., Khosravi, A., Bernard, S., Mold, J.E., Salehpour, M., Alkass, K., Perl, S., Tisdale, J., Possnert, G., Druid, H., and Frisén, J. (2017). The lifespan and turnover of microglia in the human brain. Cell Rep. *20*, 779–784.

Salehpour, M., Håkansson, K., and Possnert, G. (2015). Small sample Accelerator mass spectrometry for biomedical applications. Nucl. Instrum. Methods Phys. Res. B *361*, 43–47.

Schaub, J.R., Malato, Y., Gormond, C., and Willenbring, H. (2014). Evidence against a stem cell origin of new hepatocytes in a common mouse model of chronic liver injury. Cell Rep. *8*, 933–939.

Schittler, D., Allgöwer, F., and De Boer, R.J. (2013). A new model to simulate and analyze proliferating cell populations in BrdU labeling experiments. BMC Syst. Biol. *7*, S4.

Si-Tayeb, K., Noto, F.K., Nagaoka, M., Li, J., Battle, M.A., Duris, C., North, P.E., Dalton, S., and Duncan, S.A. (2010). Highly efficient generation of human hepatocyte-like cells from induced pluripotent stem cells. Hepatology *51*, 297–305.

Sladky, V.C., Knapp, K., Soratroi, C., Heppke, J., Eichin, F., Rocamora-Reverte, L., Szabo, T.G., Bongiovanni, L., Westendorp, B., Moreno, E., et al. (2020). E2F-family members engage the PIDDosome to limit hepatocyte ploidy in liver development and regeneration. Dev. Cell *52*, 335–349.e7.

Spalding, K.L., Arner, E., Westermark, P.O., Bernard, S., Buchholz, B.A., Bergmann, O., Blomqvist, L., Hoffstedt, J., Näslund, E., Britton, T., et al. (2008). Dynamics of fat cell turnover in humans. Nature *453*, 783–787.

Spalding, K.L., Bergmann, O., Alkass, K., Bernard, S., Salehpour, M., Huttner, H.B., Boström, E., Westerlund, I., Vial, C., Buchholz, B.A., et al. (2013). Dynamics of hippocampal neurogenesis in adult humans. Cell *153*, 1219–1227.

Spalding, K.L., Bhardwaj, R.D., Buchholz, B.A., Druid, H., and Frisén, J. (2005). Retrospective birth dating of cells in humans. Cell *122*, 133–143.

Storchova, Z., and Pellman, D. (2004). From polyploidy to aneuploidy, genome instability and cancer. Nat. Rev. Mol. Cell Biol. *5*, 45–54.

Sun, T., Pikiolek, M., Orsini, V., Bergling, S., Holwerda, S., Morelli, L., Hoppe, P.S., Planas-Paz, L., Yang, Y., Ruffner, H., et al. (2020). AXIN2+ pericentral hepatocytes have limited contributions to liver homeostasis and regeneration. Cell Stem Cell *26*, 97–107.e6.

Tanami, S., Ben-Moshe, S., Elkayam, A., Mayo, A., Bahar Halpern, K., and Itzkovitz, S. (2017). Dynamic zonation of liver polyploidy. Cell Tissue Res. *368*, 405–410.

Vansaun, M.N., Mendonsa, A.M., and Lee Gorden, D. (2013). Hepatocellular proliferation correlates with inflammatory cell and cytokine changes in a murine model of nonalchoholic fatty liver disease. PLoS ONE *8*, e73054.

Vehtari, A., Gelman, A., and Gabry, J. (2017). Practical Bayesian model evaluation using leave-one-out cross-validation and WAIC. Stat. Comput. *27*, 1413–1432.

Virtanen, P., Gommers, R., Oliphant, T.E., Haberland, M., Reddy, T., Cournapeau, D., Burovski, E., Peterson, P., Weckesser, W., Bright, J., et al. (2020). SciPy 1.0: fundamental algorithms for scientific computing in Python. Nat. Methods *17*, 261–272.

Wang, B., Zhao, L., Fish, M., Logan, C.Y., and Nusse, R. (2015). Self-renewing diploid Axin2(+) cells fuel homeostatic renewal of the liver. Nature *524*, 180–185.

Wang, M.J., Chen, F., Li, J.X., Liu, C.C., Zhang, H.B., Xia, Y., Yu, B., You, P., Xiang, D., Lu, L., et al. (2014). Reversal of hepatocyte senescence after continuous in vivo cell proliferation. Hepatology *60*, 349–361.

Wang, Y., Huang, X., He, L., Pu, W., Li, Y., Liu, Q., Li, Y., Zhang, L., Yu, W., Zhao, H., et al. (2017). Genetic tracing of hepatocytes in liver homeostasis, injury, and regeneration. J. Biol. Chem. *292*, 8594–8604.

Watanabe, T., and Tanaka, Y. (1982). Age-related alterations in the size of human hepatocytes. A study of mononuclear and binucleate cells. Virchows Arch. B Cell Pathol. Incl. Mol. Pathol. *39*, 9–20.

Wei, Y., Wang, Y.G., Jia, Y., Li, L., Yoon, J., Zhang, S., Wang, Z., Zhang, Y., Zhu, M., Sharma, T., et al. (2021). Liver homeostasis is maintained by midlobular zone 2 hepatocytes. Science *371*, eabb1625.

Wilkinson, P.D., Delgado, E.R., Alencastro, F., Leek, M.P., Roy, N., Weirich, M.P., Stahl, E.C., Otero, P.A., Chen, M.I., Brown, W.K., and Duncan, A.W. (2019). The polyploid state restricts hepatocyte proliferation and liver regeneration in mice. Hepatology *69*, 1242–1258.

Yanger, K., Knigin, D., Zong, Y., Maggs, L., Gu, G., Akiyama, H., Pikarsky, E., and Stanger, B.Z. (2014). Adult hepatocytes are generated by self-duplication rather than stem cell differentiation. Cell Stem Cell *15*, 340–349.

Yeung, M.S., Zdunek, S., Bergmann, O., Bernard, S., Salehpour, M., Alkass, K., Perl, S., Tisdale, J., Possnert, G., Brundin, L., et al. (2014). Dynamics of oligodendrocyte generation and myelination in the human brain. Cell *159*, 766–774.

Yeung, M.S.Y., Djelloul, M., Steiner, E., Bernard, S., Salehpour, M., Possnert, G., Brundin, L., and Frisén, J. (2019). Dynamics of oligodendrocyte generation in multiple sclerosis. Nature *566*, 538–542.

Zhang, S., Zhou, K., Luo, X., Li, L., Tu, H.-C., Sehgal, A., Nguyen, L.H., Zhang, Y., Gopal, P., Tarlow, B.D., et al. (2018). The polyploid state plays a tumor-suppressive role in the liver. Dev. Cell *44*, 447–459.e5.

STAR★METHODS

KEY RESOURCES TABLE

REAGENT or RESOURCE	SOURCE	IDENTIFIER
Antibodies		
Arginase-1	Sigma Aldrich	HPA024006; RRID: AB_1844987
Cytokeratin 19	Invitrogen	MA5-12663; RRID: AB_10984317
HNF4α	Santa Cruz	sc-374229; RRID: AB_10989766
Ki-67	Abcam	ab16667; RRID: AB_302459
Ki-67	Dako	M7240; RRID: AB_2142367
Prox1	Abcam	ab11941; RRID: AB_298722
Slc2a2	Atlas Antibodies	HPA028997; RRID: AB_2672860
Biological samples		
Post mortem liver tissue	Department of Oncology-Pathology, Karolinska Institutet	https://ki.se/
Surgical liver biopsies	University Hospital Carl Gustav Carus Dresden	https://www.uniklinikum-dresden.de/de
Frozen primary human hepatocytes	Leipzig University Hospital	https://www.uniklinikum-leipzig.de/
Deposited data		
^{14}C data	This paper	Table S2
Model selection and parameter estimates	This paper	Table S3
Software and algorithms		
ImageJ (version 1.52p)	Wayne Rasband and contributors National Institutes of Health, USA	https://imagej.nih.gov/ij/
CellProfiler (version 4.2.1)	Broad Institute, Inc.	https://cellprofiler.org/
VIS-Zeiss-LSM-Plugin (version 5.3.1.1723)	Visiopharm®	https://visiopharm.com/
CellProfiler pipeline	Zenodo	https://doi.org/10.5281/zenodo.6448136
Python (version 3.7.4), with packages -arviz (0.11.2) -emcee (3.0.2) -numpy (1.18.3) -scipy (1.7.2) -matplotlib (3.1.2)	Python Software Foundation	https://www.python.org/
Source code for parameter estimation and simulation	Zenodo	https://doi.org/10.5281/zenodo.6448136
Graphical Abstract	BioRender	https://biorender.com/

RESOURCE AVAILABILITY

Lead contact

Further information and requests for resources and reagents should be directed to and will be fulfilled by the lead contact, Olaf Bergmann (olaf_bergmann@tu-dresden.de).

Materials availability

This study did not generate new materials.

Data and code availability

- All experimental data reported in this paper will be shared by the lead contact upon request.
- All original code has been deposited at Zenodo and is publicly available as of the date of publication. DOIs are listed in the key resources table.
- Any additional information required to reanalyze the data reported in this paper is available from the lead contact upon request.

EXPERIMENTAL MODEL AND SUBJECT DETAILS

Nondiseased human liver tissues were obtained by KI Donatum after informed consent from the individual or next of kin from 32 autopsies between 2004 and 2018 from the Swedish National Department of Forensic Medicine and from twelve patients who underwent liver resection surgery in 2017 and 2018 at the University Hospital Carl Gustav Carus Dresden (Table S1). Ethical permission for these studies was granted by the regional ethics review board in Stockholm (Dnr 2005/1029-31/2 and Dnr 2010/313-31), and the Ethikkommission an der TU Dresden (EK 365082016 and EK251062017). The liver tissues were frozen and stored at -80 °C until further analysis. Nine liver tissue samples for liver cell isolation were obtained between 2018 and 2020 from macroscopically healthy tissue that remained from resected human liver of patients with primary or secondary liver tumors or benign local liver diseases. Informed consent of the patients for the use of tissue for research purposes was obtained according to the ethical guidelines of Leipzig University Hospital (177/16-lk, 2016/07/12 and 322/17-ek 2020/06/10).

	Gender	Age (years)
Post mortem tissue	female = 10	25-79
n = 32	male = 22	20-82
Surgical biopsies	female = 7	42-82
n = 12	male = 5	58-84
Primary hepatocytes	female = 4	55-68
n = 9	male = 5	58-79

METHOD DETAILS

Isolation and cryopreservation of PHH

All media, solutions and materials used for this cell isolation procedure were sterilized by filtration or by autoclaving and every cell culture work was performed under laminar flow cabinets. The isolation of PHH with high purity (> 92%) from liver tissue samples was performed as described (Kegel et al., 2016). The protocol was modified by adding glucose and insulin to the Perfusion solution I as described by Damm et al. (Damm et al., 2019). In brief, PHHs were isolated by a two-step EGTA/collagenase perfusion technique. After isolation, PHHs were pooled, washed with PBS supplemented with calcium and magnesium ions and the number as well as the viability of cells were determined using the trypan blue exclusion technique. Based on the cell count, the number of vials and the number of cells per vial were defined ($2*10^6$ to $1*10^7$ PHH per ml Cryopreservation Medium). The following steps were always performed on ice and coolable racks for CryoVials, cold solutions as well as precooled freezing containers (4°C) were used. The appropriate cell number was transferred into a new centrifugation tube and centrifuged again for 5 min at 50 xg and 4°C. The resulting cell pellet was resuspended with the appropriate volume of PHH Cryopreservation Medium (70 % ChillProtec® plus-Medium, 20 % FBS Superior, 10 % DMSO) and suspension was quickly transferred into CryoVials. Afterwards, vials were closed, inverted briefly and transferred into a precooled freezing container as fast as possible. The freezing container filled with isopropyl alcohol provides a repeatable -1°C/min cooling rate and thus optimal conditions for successful cell cryopreservation and recovery. This container was stored quickly at -80°C for at least 24 hours before the cells were transferred to liquid nitrogen, -196°C for long-term storage.

Nucleus isolation

All steps were carried out at 4 °C. Approximately 4 g of liver tissue was homogenized in 200 ml of lysis buffer (0.32 M sucrose, 10 mM Tris-HCl, 5 mM $CaCl_2$, 5 mM MgAc, 2 mM EDTA) using a domestic blender and dounce homogenizer. Samples were then suspended in sucrose solution (2.1 M sucrose, 10 mM Tris-HCl, 5 mM MgAc), layered onto cushions of pure sucrose solution and centrifuged for 1 h at 26,500 xg. The isolated nuclei were then resuspended in nuclear storage buffer (0.44 M sucrose, 10 mM Tris-HCl, 70 mM KCl, 10 mM $MgCl_2$, 2 mM EDTA).

Flow cytometry analysis and sorting

All steps were carried out at 4 °C. For flow cytometry-based sorts of isolated nuclei, nuclei were stained overnight with HNF4α-antibody (Santa Cruz, sc-374229, RRID: AB_10989766) 1:1000, followed by 1 h incubation with Alexa Fluor-488 coupled secondary antibody (Jackson Immuno Research, 715-546-151, RRID: AB_2340850) 1:1000. DRAQ5 (Biostatus, DR51000) 1:5000 was added as nuclear stain directly before the analysis. Frozen PHH were thawed in a waterbath, washed once with 2mM EDTA, 1% BSA, in PBS and incubated with Vybrant™ DyeCycle™ Violet Stain (Invitrogen™, V35003) 1:1000 for at least 4 h.

Liver cell nuclei and PHHs were analyzed with a BD FACSAria™ II, III or Fusion. Singlets were identified and gated using FSC and SSC. Hepatocyte nuclei were identified and sorted based on their increased Alexa Fluor-488 fluorescence intensity. Separation of diploid and polyploid hepatocyte nuclei (Figure 3C) and hepatocytes (Figure 3E) was based on DNA intensity. Purities of the sorted populations were confirmed by reanalyses (Figures S1A, S3I, and S3J). Due to impurities, the measured ^{14}C levels are actually a mixture of hepatocyte and nonhepatocyte ^{14}C concentrations. For a paired measurement in hepatocytes and nonhepatocytes from the same individual, the purity-corrected ^{14}C concentration was computed by solving the equations

$$c_{\mathrm{hepato}}^{\mathrm{measured}} = p_{\mathrm{hepato}} c_{\mathrm{hepato}}^{\mathrm{corrected}} + \left(1 - p_{\mathrm{hepato}}\right) c_{\mathrm{non-hepato}}^{\mathrm{corrected}},$$

$$c_{\mathrm{non-hepato}}^{\mathrm{measured}} = p_{\mathrm{non-hepato}} c_{\mathrm{non-hepato}}^{\mathrm{corrected}} + \left(1 - p_{\mathrm{non-hepato}}\right) c_{\mathrm{hepato}}^{\mathrm{corrected}},$$

for the corrected ^{14}C concentrations $c_{\mathrm{hepato}}^{\mathrm{corrected}}$ and $c_{\mathrm{non-hepato}}^{\mathrm{corrected}}$. In the equations, p_{hepato} and $p_{\mathrm{non-hepato}}$ are the purities of the hepatocyte and the nonhepatocyte populations. Similarly, diploid and polyploid hepatocyte (nuclei) samples were corrected for purity for paired measurements. In this case, the above equations were changed to reflect that tetraploid cells contain twice as much DNA as diploid cells. The sorted liver cell nuclear pellets PHH were frozen at −20 °C until further processing.

DNA extraction from nuclei

All steps were performed under clean room conditions to prevent any carbon contamination of the samples. To extract DNA from isolated nuclei, 500 µl DNA lysis buffer (1% SDS, 5 mM EDTA-Na2, 10 mM Tris-HCl, in UltraPure™ distilled water) and 6 µl proteinase K (20 mg/ml) were added to the samples and incubated overnight at 64 °C. Half the volume of 5 M NaCl was added. Then, the samples were agitated for 15 s and centrifuged for 3 min at 16000 xg. Supernatants were transferred into glass tubes, 3× 96% ethanol was added, and DNA was precipitated by inversion. Subsequently, DNA precipitates were washed three times in washing buffer (70% EtOH, 0.5 M NaCl, in UltraPure™ distilled water) and dissolved in 500 µl UltraPure™ distilled water. DNA quantity and purity were assessed with UV spectroscopy (NanoDrop).

DNA extraction from PHH

1 ml Lysis Buffer (4 M urea, 1% Triton X-100, 10 mM EDTA, 100 mM NaCl, 10 mM Tris-HCl, pH 8.0, 10 mM dithiothreitol) supplemented with 20 µl proteinase K was added to each sample and incubated overnight at 64 °C on a shaker. The following day, 20 µl RNase Cocktail was added to the samples, which were then incubated for 1 h at 64 °C. Subsequently, samples were transferred into DNA low-bind Eppendorf tubes, spun for 60 min at 16,900 xg and supernatants collected in clean vials. The MOPS and NaCl concentration of the samples were adjusted to 50 mM and 750 mM, respectively. Qiagen genomic DNA columns were hydrated and cleaned with 10 ml Buffer B (750 mM NaCl, 50 mM MOPS, 15% ethanol, 0.15% Triton X-100, pH 7.0) before the DNA samples were transferred onto them. The columns were then washed twice with Buffer C (1 M NaCl, 50 mM MOPS, 15% ethanol, pH 7.0) and the DNA eluted with 10 ml Buffer λ (1.25 M NaCl, 50 mM MOPS, 15% ethanol, pH 8.0). 10 mL of ice-cold, 100% isopropanol was added to the eluate and the mixture was incubated at -20 °C overnight to precipitate the DNA. The following day, the tubes were centrifuged at 4,700 xg for 1 h at 4 °C. The pelleted DNA precipitate was moved into an Eppendorf tube and washed three times with 70% ethanol. After the last washing step, the DNA pellet was dried and redissolved in 200 µl distilled water. The tubes were then transferred into a dust-free facility. The DNA solution was pipetted into pre-baked glass vials and the liquid was let to evaporate at 64 °C overnight. The following day, 500 µL UltraPure™ distilled water was added to the vials and the DNA was redissolved at 64 °C for at least 1 h. In order to assess DNA concentration and purity, UV absorbance at 260 and 280 nm was measured for all DNA samples. The vials were stored frozen at -20 °C until they were submitted to AMS measurement.

Accelerator mass spectrometry (AMS)

Purified DNA samples were analyzed blindly with AMS as described previously (Spalding et al., 2013). The DNA samples were lyophilized to dryness and reduced to graphite, and $^{14}C/^{12}C$ ratios were measured at the Department of Physics and Astronomy, Applied Nuclear Physics, Ion Physics, Uppsala University, Sweden, using a 170 kV commercial MICADAS accelerator mass spectrometer (IonPlus AG, Zurich, Switzerland). The carbon background was subtracted, as described previously (Salehpour et al., 2015; Spalding et al., 2013). All ^{14}C data are reported as $\Delta^{14}C$, and the 2σ-measurement error is given (Table S2).

Immunohistochemistry (IHC)

Four percent paraformaldehyde-fixed human liver tissues were either paraffin embedded or frozen. Sections were cut at thicknesses of 6 µm (paraffin) and 40 µm (cryo). Paraffin sections were deparaffinized and rehydrated, and antigens were retrieved by 20 min incubation in boiling 0.05% citraconic anhydride buffer. The sections were incubated overnight with primary antibodies, followed by 1 h incubation with secondary antibodies. The HNF4α signal was amplified using a Tyramide Super Boost Kit (Life Technologies, B40933). Nuclei were counterstained with DRAQ5 (Biostatus, DR51000) 1:500. Images were collected with Apotome or LSM.

To assess the fraction of cycling hepatocytes in homeostasis (Figure S1C), tissue sections were stained with primary antibodies against HNF4α/Prox1 and Ki-67. Images were collected with Apotome. 9007 ± 1197 HNF4α/Prox1+ nuclei were manually evaluated for double positivity with Ki-67 using ImageJ software (version 1.52p).

Primary antibodies for IHC

Antigen	Company	Catalog Number	Dilution	RRID
Arginase-1	Sigma Aldrich	HPA024006	1:1000	AB_1844987
Cytokeratin 19	Invitrogen	MA5-12663	1:500	AB_10984317
HNF4α	Santa Cruz	sc-374229	1:500	AB_10989766
Ki-67	Abcam	ab16667	1:1000	AB_302459
Ki-67	Dako	M7240	1:100	AB_2142367
Prox1	Abcam	ab11941	1:800	AB_298722
Slc2a2	Atlas Antibodies	HPA028997	1:1000	AB_2672860

Secondary antibodies for IHC

Antigen	Conjugate	Company	Catalog Number	Dilution	RRID
Anti-Mouse IgG (H+L)	Alexa Fluor® 555	Abcam	ab150110	1:250	AB_2783637
Anti-Mouse IgG (H+L)	Biotin-SP (long spacer)	Jackson Immuno Research	715-066-151	1:250	AB_2340788
Anti-Rabbit IgG (H+L)	Alexa Fluor® 555	Abcam	ab150062	1:100	AB_2801638
Anti-Rabbit IgG (H+L)	Alexa Fluor® 488	Jackson Immuno Research	711-546-152	1:250	AB_2340619

Cell isolation from liver tissue and immunolabeling

Fresh and frozen liver samples were kept on ice, cut into small pieces, fixed in four percent paraformaldehyde and digested overnight at 37 °C (1.5 mg/ml collagenase B, 2.0 mg/ml collagenase D, in PBS) (Liu et al., 2021).

To assess the hepatocyte fraction of the isolated cells, they were incubated with Slc2a2 primary antibody (HPA028997, 1:500) overnight and AF488-coupled secondary antibody (711-546-152, 1:250) for 1 h. Nuclei were counterstained with Vybrant DyeCycle Violet Stain (Invitrogen, V35003). Cells were applied to slides and the fluorescence signal of 771 ± 7 cells assessed manually with Apotome. Slc2a2 fluorescence signal was observed as abundant membrane staining and small bright dots on the cell surface (Figure S3B). This fluorescence pattern was not detected in a negative control without primary antibody.

Automated determination of ploidy distribution

Hepatocyte ploidy classes were assessed in isolated cells from digested liver tissue (n = 30, see above) and from cryopreserved PHH (n = 7). Nuclei were counterstained with Vybrant DyeCycle Violet Stain (Invitrogen, V35003), and cells applied to slides. At least 15 images were taken per sample with a Keyence BZ-X800e microscope at 20x magnification and analyzed for their ploidy distribution using CellProfiler software (version 4.2.1). Nuclear ploidy was assigned based on the integrated fluorescence intensity, with individual cut-offs set according to their DNA intensity histograms (Figure S3D). Binucleation was determined using the minimal distance to a neighboring nucleus (empirically set to 2.8 μm) (Figure S3C). In average 5067 ± 2987 hepatocytes were classified per sample. To validate the experimental strategy, we compared this automated approach to 3D imaging (see below) (n = 5, Figure S3E upper panel) and FACS-observed ploidy levels (n = 30, Figure S3E lower panel) using Bland-Altman-analyses and observed similar results. We only included data points that ranged in the 95%- confidence interval. The CellProfiler pipeline is available in Zenodo (see key resources table). For our mathematical model, we used the measured fractions of mononucleated diploid (2n) binucleated diploid (2x2n) and mononucleated tetraploid hepatocytes (4n) to describe the change of ploidy in the human liver over lifetime (Figure 3B). Using linear regression, we determine the following functions for the ploidy:

$$p(t) = -5.16 * 10^{-3}\, t + 0.921, \quad \text{(Equation 1)}$$

$$p_{2\times 2n}(t) = 1.67 * 10^{-3}\, t + 7.36 * 10^{-2}, \quad \text{(Equation 2)}$$

$$p_{4n}(t) = 1 - p(t) - p_{2x2n}(t). \quad \text{(Equation 3)}$$

3D image analysis of hepatocyte ploidy

Immunohistochemistry was performed on 40 μm thick human liver sections. First, we visualized all nuclei (DRAQ5) and hepatocyte nuclei specifically (HNF4α) (n = 4). An LSM confocal microscope (63x oil objective) was used to take image stacks with z spacing 0.5 μm. 409 ± 122 nuclei were automatically analyzed for their fluorescence intensity and size using ImageJ software (version 1.52p), confirming a correlation of these two characteristics (Figure S3F).

For stereological analyses, the LSM confocal microscope was used in conjunction with the VIS-Zeiss-LSM-Plugin (version 5.3.1.1723). 40 μm tissue samples were stained for nuclei (DRAQ5) and hepatocyte membranes (Slc2a2), and an automated meandering algorithm was applied to randomly choose fields of view. For integrated analysis of nuclear and cell ploidy, all Slc2a2-positive hepatocytes, with complete cell bodies present in the tissue section, were examined in one field of view. Multinucleation was visually determined utilizing Slc2a2 membrane staining by zooming through the optical layers of the section. Furthermore, hepatocyte nucleus diameters were measured at the maximal cross-sectional area. In total 102 ± 2 hepatocytes had been studied per sample (n = 5). To assign the nuclei to different ploidy classes based on their size (Bou-Nader et al., 2020; Tanami et al., 2017; Watanabe and Tanaka, 1982), a cluster analysis was performed for each individual case. The nuclear volumes were normalized to the modal values, and cut-offs were set to 1.5x (2n <> 4n), 3x (4n <> 8n) and 6× mode (8n <> 16n).

Analysis of hepatocyte DNA density

To study the amount of hepatocyte DNA in the liver the density of hepatocyte nuclei was measured. Hepatocytes were labelled in 40 μm tissue sections with HNF4α or Slc2a2 (Figure 3A). The counting tool and optical dissector of the VIS-Zeiss-LSM-Plugin (version 5.3.1.1723) were applied, enabling to record hepatocyte nuclei in a defined volume. Per sample three different regions of interest were studied with at least ten fields of view randomly chosen by an automated meander algorithm (in total 758 ± 144 nuclei per sample). The measured nuclei density $\rho_{nuclei}^{measured}$ (nuclei / mm^3) (Figure S4B) was calculated into a DNA density $\rho_{DNA}^{calculated}$ (equivalents of diploid nuclei / mm^3) (Figure S4C) using the FACS-observed fractions of nuclear ploidy classes $2n_{FACS}$, $4n_{FACS}$, $8n_{FACS}$ (Figure S3G) from the very same sample, by solving the equation

$$\rho_{DNA}^{calculated} = \rho_{nuclei}^{measured}(2n_{FACS} * 1 + 4n_{FACS} * 2 + 8n_{FACS} * 4).$$

Analysis of human liver size

To characterize the size of the liver over the human life span, documented liver weights were obtained from 259 autopsies performed at the Swedish National Department of Forensic Medicine between 2003 and 2020. Informed consent was given. Ethical permission for these studies was granted by the regional ethics review board in Stockholm (Dnr 2005/1029-31/2 and Dnr 2010/313-31). Only individuals with non-diseased livers, and a BMI between 18.5 and 30.0 were included. Pediatric data are taken from (Johnson et al., 2005). To adjust weight and volume data a liver organ density of 1.08 kg/L was assumed (Heinemann et al., 1999; Johnson et al., 2005).

A universal b-spline of 2nd degree was fitted to collected data points of the liver volume (Figure S4A, n = 472). The b-spline has the following parameters: positions of interior knot points: 0, 0, 0, 30, 60, 95, 95, 95; spline control points: 0.17, 1.42, 1.79, 1.44, 1.20, 0, 0, 0.

Mathematical modeling of ^{14}C dynamics

In the following, we derive the mathematical models, describe the methods for parameter estimation and model selection, and present the results that were based on the models in detail.

We develop a mathematical model that predicts the genomic ^{14}C concentration dynamics for a self-renewing cell population. To date, label concentration dynamics have been modeled with age-, concentration- and division-structured cell populations (Bernard et al., 2010; Hasenauer et al., 2012; Hross and Hasenauer, 2016; Schittler et al., 2013). In particular, the dynamics of ^{14}C concentrations were modeled with an age-structured cell population, assuming that mainly a rapidly cycling stem cell population contributes to tissue homeostasis (Réu et al., 2017; Spalding et al., 2013; Yeung et al., 2019). Instead, our model rests upon the assumption that hepatocytes are self-renewing cells, as demonstrated in several recent reports (Malato et al., 2011; Schaub et al., 2014; Wang et al., 2017; Yanger et al., 2014).

We describe the state of a cell population i with a density in the ^{14}C concentration space, n_i(c), where n_i is the density of cells with ^{14}C concentration c. Cells divide at rate $\beta_i(t)$ and die at rate $\delta_i(t)$. We model the cell density dynamics in a subject with the following population balance equation:

$$\frac{\partial n_i(c)}{\partial t} = \overbrace{2\beta_i(t)\int dc'\, f(c,c'|c_a(t+b))\, n_i(c')}^{\text{cell birth by division}} - \overbrace{(\beta_i(t)+\delta_i(t))\, n_i(c)}^{\text{cell loss by division and death}},$$

where $c_a(t+b)$ is the atmospheric ^{14}C concentration adjusted for one year of delay along the food chain (see below), b is the time of birth, and t is the age of the subject. The kernel $f(c,c'|c_a(t+b))$ describes the fraction of dividing cells with ^{14}C concentration c' that become cells with ^{14}C concentration c given an atmospheric ^{14}C concentration of $c_a(t+b)$. We assume that new DNA, which is synthesized during DNA duplication in the cell cycle, has an atmospheric ^{14}C concentration. Then, the mean ^{14}C concentration of the two daughter cells is $\frac{c'+c_a(t+b)}{2}$. To fulfil this condition, the kernel must be symmetric around $\frac{c'+c_a(t+b)}{2}$, i.e.,

$$f\left(\frac{c'+c_a(t+b)}{2} - x, c' \middle| c_a(t+b)\right) = f\left(\frac{c'+c_a(t+b)}{2} + x, c' \middle| c_a(t+b)\right).$$

Furthermore, the kernel is cell number conserving, i.e.,

$$\int_0^\infty dc\, f(c,c'|c_a(t+b)) = 1.$$

In scenario POP1 (Figure S4E), there is only one population of cells that die at constant rates. The total number of cells $N(t) = \int_0^\infty dc\, n(c) \sim DNA(t)$ is proportional to the total amount of DNA (see above) in the case of the one population scenario. Without restriction of generality, we set this proportionality factor to one. Using this known development of the population size, we can determine the birth rate: $\beta(t) = \delta + \partial_t N(t)/N(t)$. Overall, the dynamics are described by a single turnover rate that depends on the cell death rate and number of cells. Now, we can derive the ordinary differential equation:

$$\frac{\partial \overline{c}}{\partial t} = \beta(t)\,(c_a(t+b) - \overline{c}),$$

for the mean ^{14}C concentration $\overline{c} = \int_0^\infty dc\, c\, n(c)$.

Furthermore, we define a more complex scenario POP3p (Figures 4A and S4E) that accounts for the fact that hepatocytes exist in different states of ploidy. As most polyploid hepatocytes are tetraploid (Figures 3B and S3H), we neglected higher ploidy levels, and model a mononucleated diploid (2n), binucleated diploid (2x2n) and mononucleated tetraploid cell population (4n). In this scenario, cell turnover occurs due to (a) cell division at rates β_{2n}, β_{2x2n} and β_{4n} for 2n, 2x2n and 4n hepatocytes, respectively; (b) cell death at rates δ_{2n}, δ_{2x2n} and δ_{4n} for 2n, 2x2n and 4n hepatocytes, respectively; and (c) exchange between the ploidy populations whereby the cells have to go through mitosis before they can change their population. A 2n cell can only convert to one 2x2n cell with rate $\kappa_{2n>2x2n}$. A 2x2n cell can convert to four 2n cells (rate $\kappa_{2x2n>2n}$) or two 4n cells (rate $\kappa_{2x2n>4n}$). Similarly, a 4n cell can convert to four 2n cells (rate $\kappa_{4n>2n}$) or two 2x2n cells (rate $\kappa_{4n>2x2n}$). After S-phase binucleated diploid and mononucleated tetraploid hepatocytes have eight complete sets of chromosomes. We assume that they are indistinguishable in that after that phase. Therefore, the probability of becoming a 2n, 2x2n or 4n cell is independent of whether the cell was a binucleated diploid or a mononucleated tetraploid. This allows us to eliminate two rates:

$$\beta_{2x2n} = \kappa_{4n>2x2n}\frac{\kappa_{2x2n>2n}}{\kappa_{4n>2n}}, \qquad \text{(Equation 4)}$$

$$\kappa_{2x2n>4n} = \beta_{4n}\frac{\kappa_{2x2n>2n}}{\kappa_{4n>2n}}. \qquad \text{(Equation 5)}$$

We derive the population balance equations (the arguments for the kernel functions $f(c,c'|c_a(t+b))$ and $g(c,c'|c_a(t+b))$ are skipped)

$$\frac{\partial n_{2n}(c)}{\partial t} = \overbrace{2\beta_{2n}\int dc' f n_{2n}(c')}^{\text{cell birth by division}} + \overbrace{4\kappa_{2x2n>2n}\int dc' f\, n_{2x2n}(c') + 4\kappa_{4n>2n}\int dc' f n_{4n}(c')}^{\text{ploidy decrease of 2x2n and 4n cells}} - \overbrace{(\beta_{2n}+\delta_{2n}+\kappa_{2n>2x2n})n_{2n}(c)}^{\text{cell loss due to division, death and ploidy increase}}, \qquad \text{(Equation 6)}$$

$$\frac{\partial n_{2x2n}(c)}{\partial t} = \overbrace{2\beta_{2x2n}\int dc' f\, n_{2x2n}(c')}^{\text{cell birth by division}} + \overbrace{\kappa_{2n>2x2n}\int dc' g\, n_{2n}(c')}^{\text{unfinished division of 2n cells}} + \overbrace{2\,\kappa_{4n>2x2n}\int dc' f\, n_{4n}(c')}^{\text{conversion from 4n cells}} - \overbrace{(\beta_{2x2n}+\delta_{2x2n}+\kappa_{2x2n>2n}+\kappa_{2x2n>4n})n_{2x2n}(c)}^{\text{cell loss due to division, death and ploidy change}}, \qquad \text{(Equation 7)}$$

$$\frac{\partial n_{4n}(c)}{\partial t} = \overbrace{2\beta_{4n}\int dc' f n_{4n}(c')}^{\text{cell birth by division}} + \overbrace{2\,\kappa_{2x2n>4n}\int dc' f\, n_{2x2n}(c')}^{\text{conversion from 2x2n cells}} - \overbrace{(\beta_{4n}+\delta_{4n}+\kappa_{4n>2n}+\kappa_{4n>2x2n})n_{4n}(c)}^{\text{cell loss due to division, death and ploidy change}}. \qquad \text{(Equation 8)}$$

Unfinished cell divisions of 2n cells with ^{14}C concentration c' always give rise to a 2x2n cell with ^{14}C concentration $\frac{c'+c_a(t)}{2}$ and hence

$$g(c,c'|c_a(t+b)) = K\left(c - \frac{c'+c_a(t+b)}{2}\right),$$

where K is the Dirac delta function. The total cell numbers are given by

$$N_i = \int_0^\infty dc\, n_i(c)$$

and hence with (6–8):

$$\frac{dN_{2n}}{dt} = (\beta_{2n} - \delta_{2n} - \kappa_{2n>2x2n})N_{2n} + 4\kappa_{2x2n>2n}N_{2x2n} + 4\kappa_{4n>2n}N_{4n}, \quad \text{(Equation 9)}$$

$$\frac{dN_{2x2n}}{dt} = (\beta_{2x2n} - \delta_{2x2n} - \kappa_{2x2n>2n} - \kappa_{2x2n>4n})N_{2x2n} + \kappa_{2n>2x2n}N_{2n} + 2\kappa_{4n>2x2n}N_{4n}, \quad \text{(Equation 10)}$$

$$\frac{dN_{4n}}{dt} = (\beta_{4n} - \delta_{4n} - \kappa_{4n>2n} - \kappa_{4n>2x2n})N_{4n} + 2\kappa_{2x2n>4n}N_{2x2n}. \quad \text{(Equation 11)}$$

With the total amount of DNA, the ploidy curves (1–3) and the following relations:

$$N_{2n} + 2N_{2x2n} + 2N_{4n} = DNA(t),$$

$$N_{2n} + N_{2x2n} + N_{4n} = N(t),$$

$$N_{2n} = p(t)N(t), N_{2x2n} = p_{2x2n}(t)N(t), N_{4n} = (1 - p(t) - p_{2x2n}(t))N(t),$$

we can determine the population dynamics:

$$N_{2n} = DNA(t)\frac{p(t)}{2 - p(t)}$$

$$N_{2x2n} = DNA(t)\frac{p_{2x2n}(t)}{2 - p(t)}$$

$$N_{4n} = DNA(t)\frac{1 - p(t) - p_{2x2n}(t)}{2 - p(t)}$$

Using the known development of the population sizes, we can eliminate 3 rates by using (9–11):

$$\beta_{2n}(t) = \frac{(\delta_{2n} + \kappa_{2n>2x2n})N_{2n}(t) - 4\kappa_{2x2n>2n}N_{2x2n}(t) - 4\kappa_{4n>2n}N_{4n}(t) + \partial_t N_{2n}(t)}{N_{2n}(t)} \quad \text{(Equation 12)}$$

$$\kappa_{4n>2x2n}(t) = \frac{-\kappa_{2n>2x2n}N_{2n}(t) + (\delta_{2x2n} - \beta_{2x2n} + \kappa_{2x2n>2n} + \kappa_{2x2n>4n})N_{2x2n}(t) + \partial_t N_{2x2n}(t)}{2N_{4n}(t)} \quad \text{(Equation 13)}$$

$$\beta_{4n}(t) = \frac{-\kappa_{2n>2x2n}N_{2n}(t) + (\delta_{2x2n} - \beta_{2x2n} + \kappa_{2x2n>2n} - 3\kappa_{2x2n>4n})N_{2x2n}(t) + \partial_t N_{2x2n}(t)}{2N_{4n}(t)} + \frac{2(\delta_{4n} + \kappa_{4n>2n})N_{4n}(t) + 2\partial_t N_{4n}(t)}{N_{4n}(t)} \quad \text{(Equation 14)}$$

To shorten the notation the argument of the time dependent functions are skipped. The mean ^{14}C concentrations for the populations are given by

$$\overline{c}_i = \frac{\int dc c n_i(c)}{N_i}.$$

and with (6–8) this results in (arguments for $c_a(t+b)$, $N_i(t)$ and $\overline{c}_i(t)$ are skipped):

$$\partial_t \overline{c}_{2n} = \frac{\beta_{2n}c_a N_{2n} + 2\kappa_{2x2n>2n}(\overline{c}_{2x2n} + c_a)N_{2x2n} + 2\kappa_{4n>2n}(\overline{c}_p + c_a)N_{4n}}{N_{2n}} - \frac{\overline{c}_{2n}(\beta_{2n}N_{2n} + 4\kappa_{2x2n>2n}N_{2x2n} + 4\kappa_{4n>2n}N_{4n})}{N_{2n}} \quad \text{(Equation 15)}$$

$$\partial_t \overline{c}_{2x2n} = \frac{\kappa_{2n>2x2n} c_{2n} N_{2n} + c_a(\kappa_{2n>2x2n} N_{2n} + 2\beta_{2x2n} N_{2x2n}) + 2\kappa_{4n>2x2n}(\overline{c}_{4n} + c_a) N_{4n}}{2N_{2x2n}} - \frac{2\overline{c}_{2x2n}(\kappa_{2n>2x2n} N_{2n} + \beta_{2x2n} N_{2x2n} + 2\kappa_{4n>2x2n} N_{4n})}{2N_{2x2n}} \quad \text{(Equation 16)}$$

$$\partial_t \overline{c}_{4n} = \beta_{4n}(c_a - \overline{c}_p) + \frac{\kappa_{2x2n>4n}(\overline{c}_{2x2n} - 2\overline{c}_{4n} + c_a) N_{2x2n}}{N_{4n}} \quad \text{(Equation 17)}$$

The scenario POP2p is a simplified version of the POP3p scenario, where we assume that binucleated diploid (2x2n) and mononucleated tetraploid cells (4n) behave identically. Thus, they are modeled with one population $N_p = N_{2x2n} + N_{4n}$. In this scenario, cell turnover occurs due to (a) cell division at rates β_2 and β_p for diploid and polyploid hepatocytes, respectively; (b) cell death at rates δ_2 and δ_p for diploid and polyploid hepatocytes, respectively; and (c) exchange between the ploidy populations whereby diploid cells convert to polyploid cells by unfinished cell division at rate κ_{2p}, and conversely, polyploid cells convert to diploid cells at rate κ_{p2}. We derive the population balance equations

$$\frac{\partial n_2(c)}{\partial t} = \overbrace{2\beta_2 \int dc' f n_2(c')}^{\text{cell birth by division}} + \overbrace{4\kappa_{p2} \int dc' f n_p(c')}^{\text{ploidy decrease of pn cells}} - \overbrace{(\beta_2 + \delta_2 + \kappa_{2p}) n_2(c)}^{\text{cell loss due to division, death and ploidy increase}}, \quad \text{(Equation 18)}$$

$$\frac{\partial n_p(c)}{\partial t} = \overbrace{2\beta_p \int dc' f n_p(c')}^{\text{cell birth by division}} + \overbrace{\kappa_{2p} \int dc' g n_2(c')}^{\text{unfinished division of 2n cells}} - \overbrace{(\beta_p + \delta_p + \kappa_{p2}) n_p(c)}^{\text{cell loss due to division, death and ploidy decrease}}. \quad \text{(Equation 19)}$$

The derivation of the equations for the mean ^{14}C concentration follows the same principle as the one for the POP3p scenario. The population dynamics are:

$$\frac{dN_2}{dt} = (\beta_2 - \delta_2 - \kappa_{2p}) N_2 + 4\kappa_{p2} N_p, \quad \text{(Equation 20)}$$

$$\frac{dN_p}{dt} = (\beta_p - \delta_p - \kappa_{p2}) N_p + \kappa_{2p} N_2. \quad \text{(Equation 21)}$$

The population sizes develop as follows:

$$N_2 = DNA(t) \frac{p(t)}{2 - p(t)} \quad \text{(Equation 22)}$$

$$N_p = DNA(t) \frac{1 - p(t)}{2 - p(t)} \quad \text{(Equation 23)}$$

Using (20,21) two parameters can be eliminated:

$$\beta_2(t) = \frac{(\delta_2 + \kappa_{2p}) N_2(t) + \partial_t N_2(t) - 4\kappa_{p2} N_p(t),}{N_2(t)} \quad \text{(Equation 24)}$$

$$\beta_p(t) = \frac{(\delta_p + \kappa_{p2}) N_p(t) + \partial_t N_p(t) - \kappa_{2p} N_2(t),}{N_p(t)}. \quad \text{(Equation 25)}$$

The mean ^{14}C concentrations are:

$$\frac{d\overline{c}_2}{dt} = \frac{\beta_2(t)(c_a - \overline{c}_2) N_2(t) + 2\kappa_{p2}(\overline{c}_p + c_a - 2\overline{c}_2) N_p(t)}{N_2(t)}, \quad \text{(Equation 26)}$$

$$\frac{d\overline{c}_p}{dt} = \beta_p(t)(c_a - \overline{c}_p) + \frac{\kappa_{2p}(\overline{c}_2 + c_a - 2\overline{c}_p) N_2(t)}{2N_p(t)}. \quad \text{(Equation 27)}$$

For the scenario extension POP2p_stem, we included an additional inflow to diploid cells from a stem cell population (Figure S4E). We assume that the stem cells have the food chain delayed atmospheric ^{14}C concentration and their flow is constant through the lifetime. Except for the inflow term, the master equation for POP2p_stem is identical to POP2p (Equations 18 and 19).

$$\frac{\partial n_2(c)}{\partial t} = \overbrace{\lambda K(c - c_a)}^{\text{inflow from stem cells}} + \overbrace{2\beta_2 \int dc' f n_2(c')}^{\text{cell birth by division}} + \overbrace{4\kappa_{p2} \int dc' f\, n_p(c')}^{\text{ploidy decrease of pn cells}} - \overbrace{(\beta_2 + \delta_2 + \kappa_{2p}) n_2(c)}^{\text{cell loss due to division, death and ploidy increase}}, \quad \text{(Equation 26)}$$

$$\frac{\partial n_p(c)}{\partial t} = \overbrace{2\beta_p \int dc' f n_p(c')}^{\text{cell birth by division}} + \overbrace{\kappa_{2p} \int dc' g\, n_2(c')}^{\text{unfinished division of 2n cells}} - \overbrace{(\beta_p + \delta_p + \kappa_{p2}) n_p(c)}^{\text{cell loss due to division, death and ploidy decrease}} . \quad \text{(Equation 27)}$$

K is the Dirac delta function and λ determines the strength of the flow from the stem cell population to the diploid one. The population dynamics are:

$$\frac{dN_2}{dt} = \lambda + (\beta_2 - \delta_2 - \kappa_{2p}) N_2 + 4\kappa_{p2} N_p , \quad \text{(Equation 28)}$$

$$\frac{dN_p}{dt} = (\beta_p - \delta_p - \kappa_{p2}) N_p + \kappa_{2p} N_2 . \quad \text{(Equation 29)}$$

Using (20,21) two parameters can be eliminated:

$$\beta_2(t) = \frac{-\lambda + (\delta_2 + \kappa_{2p}) N_2(t) + \partial_t N_2(t) - 4\kappa_{p2} N_p(t),}{N_2(t)} \quad \text{(Equation 30)}$$

$$\beta_p(t) = \frac{(\delta_p + \kappa_{p2}) N_p(t) + \partial_t N_p(t) - \kappa_{2p} N_2(t),}{N_p(t)}. \quad \text{(Equation 31)}$$

Finally, the dynamics for the mean ^{14}C concentration are:

$$\frac{d\bar{c}_2}{dt} = \frac{(c_a - \bar{c}_2)(\lambda + \beta_2(t) N_2(t)) + 2\,\kappa_{p2}(\bar{c}_p + c_a - 2\,\bar{c}_2) N_p(t)}{N_2(t)}, \quad \text{(Equation 32)}$$

$$\frac{d\bar{c}_p}{dt} = \beta_p(t)(c_a - \bar{c}_p) + \frac{\kappa_{2p}(\bar{c}_2 + c_a - 2\,\bar{c}_p) N_2(t)}{2\,N_p(t)}. \quad \text{(Equation 33)}$$

For all scenarios, we assume that all cells have the food chain delayed atmospheric ^{14}C concentration at the time of subject birth, i.e., $\bar{c}_i(t = 0) = c_a(b)$ as the initial condition. This fully specifies the dynamics of the mean ^{14}C concentration. We would like to note that these scenarios are too complex to describe cell turnover with a simple turnover rate. We need to specify the death rates and the exchange rates to fully define the model. The time-dependent cell birth rates can then be computed using the equations above. We implemented a numerical solution of our model in Python (https://github.com/fbnrst/Heinke_2020).

Parameter estimation and model selection

Experimentally, we isolated hepatocyte nuclei or used PHH, and determined the mean ^{14}C concentrations for different mixtures of diploid and polyploid cell populations. In case of nuclei sorting, diploid nuclei (A2n) can originate from mononucleated diploid and binucleated diploid cells, and tetraploid nuclei (A4n) can originate from mono- and binucleated tetraploid hepatocytes. In case of cell sorting, diploid cells (B2n) only comprise mononucleated diploid cells, while the tetraploid hepatocyte fraction (B4n) contains binucleated diploid and mononucleated tetraploid hepatocytes. Nonploidy-sorted nuclei (C) originate from cells of all possible nucleation and ploidy levels. From scenario POP3p, we can predict the experimentally measured ^{14}C concentrations by weighting the ^{14}C concentrations $\bar{c}_2$, $\bar{c}_{2x2}$ and $\bar{c}_{4n}$ according to the relative fractions of ploidy levels in the hepatocyte populations:

$$\bar{c}(t) = \frac{w^i_{2n}\bar{c}_{2n}(t) + 2w^i_{2x2n}\bar{c}_{2x2n}(t) + 2w^i_{4n}\bar{c}_{4n}(t)}{w^i_{2n} + 2w^i_{2x2n} + 2w^i_{4n}},$$

where w^i_j are the weights of the j population for a sort of type i, and the factor 2 reflects that 2x2n and 4n cells have double the amount of DNA. The weights are given by

$$\begin{array}{lll}
w^{A2n}_{2n} = p(t), & w^{A2n}_{2x2n} = p_{2x2n}(t), & w^{A2n}_{4n} = 0, \\
w^{A4n}_{2n} = 0, & w^{A4n}_{2x2n} = 0, & w^{A4n}_{4n} = 1, \\
w^{B2n}_{2n} = 1, & w^{B2n}_{2x2n} = 0, & w^{B2n}_{4n} = 0, \\
w^{B4n}_{2n} = 0, & w^{B4n}_{2x2n} = p_{2x2n}(t), & w^{B4n}_{4n} = 1 - p(t) - p_{2\times 2n}(t), \\
w^{C}_{2n} = p(t), & w^{C}_{2x2n} = p_{2\times 2n}(t), & w^{C}_{4n} = 1 - p(t) - p_{2\times 2n}(t).
\end{array}$$

In case of the POP2p scenario the binucleated diploid and mononucleated tetraploid populations are combined to one polyploid population

$$\bar{c}(t) = \frac{w^i_{2n}\bar{c}_2(t) + 2w^i_p\bar{c}_p(t)}{w^i_{2n} + 2w^i_p}\ ,\ w^i_p = w^i_{2x2n} + w^i_{4n} .$$

For the POP1 scenario, we ignored the different ploidy compositions of the samples.

We used an additive Gaussian noise model to define a likelihood for our data. This noise has contributions from actual subject-to-subject variability and from the measurement error $\sigma_{m_k}^2$ for each sample k. We assumed that the subject-to-subject variability is constant for all samples and with a variance of σ_s^2. The combined variance of the two Gaussians is $\sigma_k^2 = \sigma_s^2 + \sigma_{m_k}^2$. We estimated parameter ranges with Bayesian inference. Depending on the model, we used uniform priors in the log space for the unknown rate parameters

$$\mathcal{U}(\log_{10}10^{-6}\mathit{years},\ \log_{10}10^{1}\mathit{years})$$

and a uniform prior for σ_s:

$$\sigma_s \sim \mathcal{U}(0,\ 0.2).$$

Due to the cell number constraints, we must eliminate a rate for each population. Mathematically, these rates can become negative. However, because a negative rate is physically not possible, an infinitely unlikely value must be defined for the likelihood. For such cases, the likelihood is set to $-\infty$.

To numerically solve the Bayesian inference problem (Fröhlich et al., 2017; Hasenauer et al., 2012; Virtanen et al., 2020), we used Markov chain Monte Carlo (MCMC) sampling as implemented in emcee: The MCMC Hammer (Foreman-Mackey et al., 2013). For each scenario, we used 3000 samples, of which 1000 were used for the burn-in phase, and the number of chains was 50 times the number of parameters resulting in 3000*50*number of parameters samples. The initial values for the unknown parameters were drawn from the priors. However, if a set of initial values results in a negative rate it is discarded, and a new sample is drawn. This avoids "stuck" chains in an area with a flat likelihood of $-\infty$.

To select the model with the highest predictive power, we employed leave-one-out cross validation (LOO). We estimated LOO from the MCMC chains using Pareto-smoothed importance sampling (Vehtari et al., 2017).

Bayesian inference results

MCMC sampling resulted in empirical distributions that approximate the posterior distributions of the estimated parameters. These posterior distributions were visualized in Figures S6A–S6F for the hepatocyte scenarios, nonhepatocytes and nonsorted liver nuclei. From these posterior distributions, we estimated parameter values and confidence intervals (Table S3). Using those point estimates, the model predictions as well as the data are shown in Figures S7A–S7C.

Hepatocytes

When using the simplest scenario POP1, we estimated a death rate of 17%/year (CI: [16%/year, 19%/year) (Table S3). With $\beta(t) = \delta + \partial_t DNA(t)/DNA(t)$, we can compute the time-dependent birth rate (Figure S4F, $\beta = 17\%/\mathit{year}$ for a 50-year-old subject).

In contrast, the most complex scenario POP3p explicitly incorporates polyploidization of the hepatocytes and distinguishes between a binucleated diploid and mononucleated tetraploid population. It produced the best fit of the data with a model weight of 52% (Table S3). The death rate of 72%/year (CI: [23%/year, 162%/year]) for the diploid population is larger than the ones for the binucleated diploid and the mononucleated tetraploid population with 0.1%/year (CI: [0%/year, 42%/year]) and 19%/year (CI: [14%/year, 29%/year]). This results in a higher turnover rate for the diploid population compared to the polyploid ones. The large confidence interval of the binucleated diploid population indicates that only an upper bound for the death rate can be determined which is similar to the one of the mononucleated tetraploid population. The exchange rates between the populations are small compared to the death rates. Diploid cells increase their ploidy with a rate of 0.02%/year (CI: [0%/year, 1.5%/year]). For the ploidy decrease from binucleated diploid cells and mononucleated tetraploid cells the rates are 0.1%/year (CI: [0.01%/year, 10%/year]) and 0.01%/year (CI: [0%/year, 0.1%/year]), respectively. Using Equations(12-14), we can compute the time-dependent birth rates (Figure 4B). They change mainly due to the alteration of the liver size. The mononucleated diploid population divides much faster ($\beta_{2n} = 71\%/\mathit{year}$ for a 50-year-old subject) than the binucleated diploid ($\beta_{2x2n} = 10\%/\mathit{year}$ for a 50-year-old subject) and the mononucleated tetraploid hepatocytes ($\beta_{4n} = 0.9\%/\mathit{year}$ for a 50-year-old subject). The large uncertainties in the exchange rates as well as the death rate for the binucleated tetraploid population make a more detailed analysis of this scenario ineffectual. However, it shows that the binucleated diploid population could behave identical to the mononucleated tetraploid.

The POP2p scenario reduces the complexity of the POP3p scenario combining the two similarly behaving polyploid populations. The scenario POP2p has a lower model weight of 28% (Table S3), but is still predicting the data well and has the benefit of much smaller confidence intervals due to the decreased complexity. It also predicts clear differences in turnover for diploid and polyploid hepatocytes with cell death rates of 72%/year (CI: [25%/year, 156%/year]) and 10%/year (CI: [6%/year, 15%/year]), respectively. Remarkably, the exchange rates between the diploid and the polyploid population are comparably low. We found 0.5%/year (CI: [0.1%/year, 1%/year] for diploid to polyploid and 1.7%/year (CI: [0.6%/year, 12%/year]) for polyploid to diploid. Using equations (24) and (25), we can compute the time-dependent birth rates (Figure S4G). Both rates change mainly due to the alteration of the liver size. The diploid population divides much faster ($\beta_2 = 68\%/\mathit{year}$ for a 50-year-old subject) than the polyploid population ($\beta_p = 11\%/\mathit{year}$ for a 50-year-old subject).

The POP2p_stem scenario is an extension of POP2p. The additional inflow of stem cells to the diploid hepatocyte population has only a small effect on the parameters estimates. The death rates are 78%/year (CI: [26%/year, 163%/year]) and 10%/year (CI: [7%/year, 16%/year]) for the diploid and polyploid hepatocytes. The exchange rates between the ploidy classes are 0.02%/year (CI: [0%/year, 3%/year] for diploid to polyploid and 0.3%/year (CI: [0.02%/year, 15%/year]) for polyploid to diploid. Despite the lower point estimates for these exchange rates the confidence intervals are similar. The flow from the stem cells to the diploid population

λ is $4 * 10^{-4}$ cells/year (CI: [0 cells/year, $3 * 10^{-3}$cells/year]). For a given age, the rate of inflowing cells is $\lambda/N_2(t)$ (see Equation 22). This corresponds to 0.043% contribution to the diploid hepatocyte compartment in a mid-aged individual (50-years-old).

We used the POP3p scenario to estimate the number of diploid and polyploid hepatocytes that are born every day. For a short time interval, t_0, these numbers can be estimated as

$$N_{2n}(t) = (2\beta_{2n}N_{2n} + 4\,\kappa_{2x2n>2n}N_{2x2n} + 4\kappa_{4n>2n}N_{4n})t_0,$$

$$N_{2x2n}(t) = (2\beta_{2x2n}N_{2x2n} + 2\,\kappa_{4n>2x2n}N_{4n})t_0,$$

$$N_{4n}(t) = (2\,\beta_{4n}N_{4n} + 2\kappa_{2x2n>4n}N_{2x2n})t_0,$$

$$N_{2n} = p(t)\,N_0,\; N_{2x2n} = p_{2x2n}(t)N_0,\; N_{4n} = N_0(1 - p_{2x2n}(t) - p(t)),$$

where N_0 is the total number of hepatocytes in the liver. N_0 was calculated for 13 patients using the formula

$$N_0 = \rho_{nuclei}\,V_{liver}\left(2n + \frac{2x2n}{2} + 4n + \frac{2x4n}{2} + 8n + \frac{2x8n}{2}\right),$$

where ρ_{nuclei} is the measured nuclei density (nuclei / l) (Figure S4B), V_{liver} the liver volume (l) (Figure S4A) and *2n*, *2x2n* … are the fractions of the respective ploidy classes (Figures 3B and S3H). Where no individual datapoints were available for the liver volume or fractions of the ploidy classes, we used an estimate according to the spline or linear fits. Based on the linear regression of this cohort, we assume that the liver of a 50 years-old person contains around 2.5×10^{11} hepatocytes (Figure S4D), in line with the literature (Nagy et al., 2020). Accordingly, we estimate that approximately 647 million mononucleated diploid, 24 million binucleated diploid and 27 million mononucleated tetraploid hepatocytes are born every day.

Nonhepatocytes and nonsorted liver nuclei

For the nonhepatocyte sorts and the nonsorted liver nuclei, we used scenario POP1 to estimate an average turnover rate. We found an average turnover rate of 14%/year (CI: [10%/year, 18%/year]) and 19%/year (CI: [16%/year, 21%/year]) for the nonhepatocyte sorts and nonsorted liver nuclei, respectively.

Simulation of cell age distribution

We simulated a single-cell-based model to compute the cell age distribution for scenario POP3p (Figures 4C–4F). The state of the model at time t is given by the birth times a_i (i=1…n), b_j (j=1…m) and c_k (k=1…l) of n diploid cells (2n), m binucleated diploid cells (2x2n) and l mononucleated tetraploid cells (4n), respectively. We simulate the dynamics with a fixed time step Δt. At each time step, the age of all cells is increased by Δt. Furthermore, the following events may occur for each cell at every time step: (a) 2n, 2x2n and 4n cells divide with probability $\beta_2(t) \times \Delta t$, $\beta_{2x2n}(t) \times \Delta t$ and $\beta_{4n}(t) \times \Delta t$, respectively. If cell division occurs, the corresponding cell is removed, and two new cells are added. (b) 2n, 2x2n and 4n cells die with probability $\delta_2 \times \Delta t$, $\delta_{2x2n} \times \Delta t$ and $\delta_{4n} \times \Delta t$, respectively. If cell death occurs, the corresponding cell is removed. (c) A 2n cell turns into a 2x2n cell with the probability $\kappa_{2n>2x2n} \times \Delta t$. (d) A 2x2n or 4n cell turns into four 2n cells with probability $\kappa_{2x2n>2n}(t) \times \Delta t$ and $\kappa_{4n>2n} \times \Delta t$. (e) A 2x2n cell turns into two 4n cells with probability $\kappa_{2x2n>4n}(t) \times \Delta t$. (f) A 4n cell turns into two 2x2n cells with probability $\kappa_{4n>2x2n}(t) \times \Delta t$. In all cases, the age of new cells is set to 0. If multiple events are selected for a single cell in a single time step, then only one of them is randomly selected with probabilities that are proportional to the corresponding rates. For a small time step Δt, the cell number dynamics of the single-cell-based model converges to the solution of equations (8-10) and (13-15). Additionally, the birth times of the cells (a_i(t), b_i(t) and c_i(t)) allow the cell age distribution to be calculated. We used the best-fit parameters for scenario POP3p (Table S3) to parameterize the model. The simulation was initialized with $10^6\,p(0)$ 2n cells $10^6\,p_{2x2n}(0)$ 2x2n cells and $10^6\,(1 - p(0) - p_{2x2n}(0))$ 4n cells. We performed the model until t = 80 years using a time step of $\Delta t = 10^{-3}$ years.

Genomic DNA repair in modeling ^{14}C measurements

To determine the influence of the DNA repair, we include the exchange of DNA due to repair in the POP1 scenario (Figures S5A and S5B). We assume that the repair leads to a continuous replacement of a small part of the DNA leading to the following master equation (see above for details):

$$\frac{\partial n(c)}{\partial t} = -(\gamma + \delta + \beta)n(c) + \gamma\int dc' \mathrm{D}(f\,c' + (1 - f)\mathrm{c_a(t)} - \mathrm{c})\mathrm{n(c')} + 2\beta\int dc' f n(c'),$$

where D is the Dirac-delta-distribution, f is the fraction of damaged DNA, and γ, δ and β are the rates for the DNA repair, cell death and cell division, respectively. From the master equation the mean ^{14}C concentrations can be calculated:

$$\frac{d\overline{c}}{dt} = \left[\beta(t) + \overbrace{\gamma(1 - f)}^{\text{effective DNA repair}}\right](c_a - \overline{c},)$$

$$\beta(t) = \delta + \partial_t N(t)/N(t)$$

On the population level, the effective DNA repair rate equals the renewal rate of the entire DNA due to DNA damage.

We used already measured ^{14}C concentrations of cortical neurons (Huttner et al., 2014; Yeung et al., 2014) to estimate the impact of DNA repair on the computed cell turnover rates. Cortical and cerebellar neurons are as old as the individual and are not exchanged throughout lifetime (Bhardwaj et al., 2006; Huttner et al., 2014; Spalding et al., 2005). Thus, all measured exchange of ^{14}C must be due to DNA repair. Using the published ^{14}C concentrations of cortical and cerebellar neurons (taken from Huttner et al., 2014, Table S3, and Yeung et al., 2014, Table S5), we estimated an effective rate of DNA repair using a constant population size. To estimate an upper limit of the potential impact of DNA repair on ^{14}C concentrations, we included only subjects older than 50 years of age having the longest history of putative DNA repair. The point estimate for the effective DNA repair rate is 0.003%/year (CI: [0%/year, 0.03%/year]) (Figure S5B). Using this point estimate, we can fit the POP1 scenario with DNA repair to our ^{14}C measurements and determine the effects of DNA repair to the death rate. Additionally, we increased the effective DNA repair up to 100-fold resulting in an upper estimate for the influence of the DNA repair.

Validity of the error model

Here, we will show that our error model is consistent with the data. For parameter estimation, we used an additive Gaussian error model that includes the reported, subject-specific ^{14}C measurement error σ_i and an *a priori* unknown additional term σ that shall reflect the effect of all other sources of variability. Hence, we assume that the residuals r_i, i.e. the difference between predicted and measured ^{14}C concentration, follow a normal distribution:

$$r_i \sim N(0, \sqrt{\sigma_i + \sigma})$$

where σ_i are the known errors from the mass-spectrometry measurement and we estimated σ when fitting the models. If we normalize the residuals, all residuals should follow the same normal distribution with standard deviation 1:

$$r_i \,/\, \sqrt{\sigma_i + \sigma} \sim N(0, 1)$$

Indeed, the normalized residuals follow this distribution reasonably well for each scenario (Figure S5C).

Influence of the food chain delay on ^{14}C birth dating

^{14}C birth dating has been used in several publications in which the accuracy of age determination has been documented in different cell types of the human body, but also verified by dating Swedish tree rings (Bergmann et al., 2015; Huttner et al., 2018; Spalding et al., 2005). The food chain delay of one year has been applied in several previous publications (mentioned above) to account for a delay in incorporating atmospheric ^{14}C into the human body. The existence of a carbon food lag is also supported by Georgiadou et al. (2013), who estimated the lag between the measured atmospheric ^{14}C concentration and the biological ^{14}C concentration to 1.5 ± 0.7 years. To test the influence of the food delay on our results, we fitted the POP1 scenario to the data using different food chain delays. In Figure S5D, the obtained point estimates and 1σ-error intervals of the turnover rate are depicted for different hypothetical food chain delays. A delay of up to 3 years would have minimal influence on the point estimate compared to the error interval, and therefore has little impact on our results.

QUANTIFICATION AND STATISTICAL ANALYSIS

Statistical analyses were performed with GraphPad (version 5.03). Details can be found in the figure legends. Numbers of technical replicates are stated in the respective methods section. A statistical difference was assumed for $p < 0.05$.

For descriptive data analyses the mean ± SD or median ± interquartile range is shown. ^{14}C measurements are reported with 2σ-confidence interval. Age-dependencies of the genomic ^{14}C age, hepatocyte ploidy fractions, fraction of FACS-isolated hepatocyte nuclei, density of hepatocyte nuclei, density of hepatocyte DNA and total hepatocyte number were analyzed with linear regressions. The differences of ^{14}C levels in hepatocyte ploidy classes were tested with paired t-test.

To select the scenario with the highest predictive power, we employed leave-one-out cross validation (LOO). The used MCMC sampling resulted in empirical distributions that approximate the posterior distributions of the estimated parameters. From these posterior distributions, we estimated parameter values and 1σ-confidence intervals. For validation of the additive Gaussian error model, the normality of the normalized residuals was tested with the Shapiro-Wilk test. Further statistical details of the mathematical modeling can be found in the methods section.